ABSTRACT

Title of thesis: DESIGN OF NANOPHOTONIC
ANTIREFLECTION COATINGS FOR
III-V THIN-FILM PHOTOVOLTAICS

Daniel Goldman, Master of Science, 2016

Thesis directed by: Professor Jeremy Munday
Department of Electrical and Computer Engineering

Thin-film photovoltaics have provided a critical design avenue to help decrease the overall cost of solar power. However, a major drawback of thin-film solar cell technology is decreased optical absorption, making compact, high-quality antireflection coatings of critical importance to ensure that all available light enters the cell. In this thesis, we describe high efficiency thin-film InP and GaAs solar cells that utilize a periodic array of nanocylinders as antireflection coatings. We use coupled optical and electrical simulations to find that these nanophotonic structures reduce the solar-weighted average reflectivity of InP and GaAs solar cells to ~ 1.3 %, outperforming the best double-layer antireflection coatings. The coupling between Mie scattering resonances and thin-film interference effects accurately describes the optical enhancement provided by the nanocylinders. The spectrally resolved reflectivity and J-V characteristics of the devices under AM1.5G solar illumination are determined via the coupled optical and electrical simulations, resulting in predicted power conversion efficiencies > 23 %. We conclude that the nanostructured coat-

ings reduce reflection without negatively affecting the electronic properties of the InP and GaAs solar cells by separating the nanostructured optical components from the active layer of the device.

DESIGN OF NANOPHOTONIC ANTIREFLECTION COATINGS FOR III-V THIN-FILM PHOTOVOLTAICS

by

Daniel Aaron Goldman

Thesis submitted to the Faculty of the Graduate School of the
University of Maryland, College Park in partial fulfillment
of the requirements for the degree of
Master of Science
2016

Advisory Committee:
Professor Jeremy Munday, Chair/Advisor
Professor Edo Waks
Dr. Amit Agrawal

Acknowledgments

I would like to take a moment to thank the following people, without whom this thesis would not be possible. Firstly, thank you to my parents, my brother, and my extended family members, who have constantly supported me in everything that I do. Next, my friends and colleagues in the Munday Lab, who were always willing to lend a helping hand and spent time chasing down software licenses for the electrical simulations of this work. In that regard, I want to particularly thank Joe Murray, who designed, ran, and analyzed the electrical simulations of this work, without whom the paper we published and this thesis would not be possible. I also want to thank my friends both at the University of Maryland and away from it, whose encouragement helped me push through the last bit of this thesis and whose support I always value. Most importantly, I would like to thank my advisor, Dr. Munday, for his patience, kindness, support, and technical advisement throughout my career here at the University of Maryland. I have learned so much from him and am eternally thankful for the opportunities and support he has provided me. Finally, I would like to thank all of my committee members for their service on my committee and for their feedback and evaluation. I hope that this work can provide a small window into the possibilities of nanostructured antireflection coatings for high-efficiency photovoltaics and help push solar energy technology further into the future.

Table of Contents

List of Tables

List of Figures

List of Abbreviations and Symbols

A	Absorption
AM1.5G	Air-Mass 1.5 Global Solar Spectrum
ARC	Antireflection Coating
CAD	Computer-Aided Design
E_g	Band Gap
η	Power Conversion Efficiency
EVA	Ethylene Vinyl Acetate
FF	Fill Factor
FIB	Focused Ion Beam
FDTD	Finite-Difference Time-Domain
GUI	Graphical User Interface
ITO	Indium-Tin-Oxide
J	Current Density
J_{sc}	Short-Circuit Current Density
λ	Wavelength
NC	Nanocylinder
NREL	National Renewable Energy Laboratory
PML	Perfectly Matched Layer
ϕ	Solar Photon Flux
R	Reflectance
SEM	Scanning Electron Microscope
TCO	Transparent Conducting Oxide
TFSF	Total-Field Scattered-Field
V	Voltage
V_{oc}	Open-Circuit Voltage

List of Publications

Portions of this thesis have been drawn from the following publications:

Daniel A. Goldman, Joseph Murray, and Jeremy N. Munday, "Nanophotonic resonators for improved InP solar cells", Optics Express, **24**(10), A925-A934 (2016).

Chapter 1:   Introduction

The field of photovoltaics has been a primary area of research for electrical engineers, materials scientists, and physicists for over five decades. From the invention of photovoltaic cells at Bell Labs in the mid-1950's, their implementation in space missions in the 1960's and 1970's, to modern day rooftop solar companies and panel manufacturers, the development and maturation of the field into a viable industry is well documented. With the ever-increasing threat of irreversible climate change, photovoltaics have now become a prominent method of alternative energy generation and production. The technological development of photovoltaic devices, also known as solar cells, is critical to combat the effects of climate change and to push our global society towards a more sustainable existence. New methods of increasing the power conversion efficiency of these devices and of minimizing the mechanisms responsible for energy loss are necessary in order to continue developing photovoltaic technology and making it more economically viable. In this section we will describe a few of these methods, the primary materials and techniques used in their implementation, and relate these ideas to the overall objectives and goals of this thesis.

1.1   Thin-Film Photovoltaics and Nanophotonics

Solar cells operate via a simple physical mechanism: the absorption of photons with energies higher than the bandgap of the semiconductor being used as the active photovoltaic material. The absorption of the photon generates an electron-hole pair, which is then separated by the internal field of the p-n junction in the device. Each individual charge carrier drifts or diffuses towards a contact, and then is extracted out of the device as DC current. The material used for the absorbing semiconductor is known as the active photovoltaic material. Typical solar cells have active material thicknesses of hundreds or thousands of μm, in order to absorb more of the light that enters the cell and provide structural rigidity. However, active material quality has a major impact on the device performance, and large single crystals of most materials used for photovoltaics (e.g. Silicon (Si), Gallium Arsenide (GaAs)) are expensive to produce. In this vein, thin-film photovoltaics have provided a critical design avenue to help decrease the overall cost of solar power. Thin-film solar cells are made with many of the same active materials as typical photovoltaic devices except they contain less of that material, with active layer thicknesses of a few μm to tens or hundreds of μm. This helps reduce the cost because less of the expensive high-quality semiconductor material is used.

However, a major drawback of thin-film solar cell technology is decreased optical absorption. A material's optical absorption is characterized by its absorption coefficient, an intrinsic material quantity which describes how far light of a certain frequency (and therefore energy) can penetrate into the material before being ab-

sorbed. This is why most conventional solar cells use thick layers of active material, in order to guarantee that incident light over the entire visible spectrum is absorbed by the cell and converted to electricity. Thin-film solar cells naturally have less material and are more likely to appear transparent to longer wavelength (lower frequency) light, thus absorbing less light and losing potential photogenerated carriers, which could be extracted for electrical power.

This behavior results in a trade-off when designing thin-film solar cells - balancing the optical performance with the electrical performance. Figure 1.1 shows
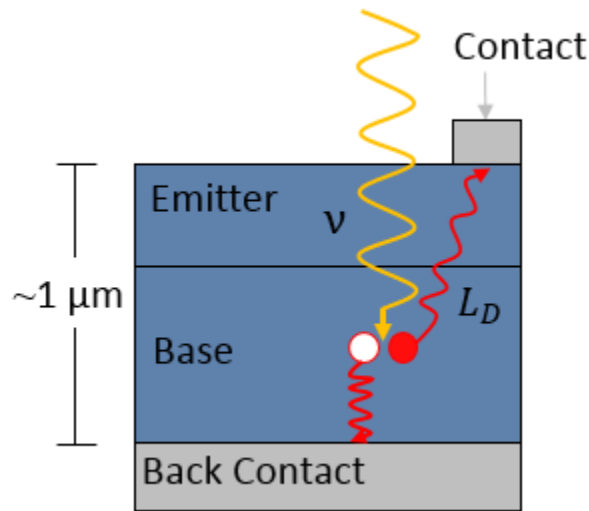
Figure 1.1: A simplified schematic of a typical thin-film solar cell. The cell consists of front and back contacts and the emitter and base layers of active material which form the p-n junction of the device. In this schematic we are assuming an n-type emitter layer and p-type base layer, consistent with the setup of many III-V solar cells. Incoming light of frequency ν is incident on the cell, generating an electron-hole pair (electron-red, hole-white). The carriers are separated by the internal field, and then the minority carriers, here the electrons, travel a distance $\leq L_D$ (the diffusion length) to be extracted as photogenerated current from the contacts.

a schematic of a typical thin-film solar cell. Here, incident light is absorbed by the cell, generating an electron-hole pair. The minority carrier, namely the carrier that has the lower concentration in the active semiconductor material (*e.g.* an electron in a p-type material), travels a distance L_D to be extracted by the contacts. L_D is the diffusion length of the minority carrier, the length the electron (or hole) can travel before it recombines. In order for the solar cell to maximize its power conversion efficiency it should be able to collect all of the carriers generated by the photons it absorbs and extract them as current. However, if the device is so thick that the distance from the junction to the contacts is larger than L_D then it may be difficult to efficiently extract the generated carriers. Additionally, the active layers must still be large enough to absorb most of the incident light, so a good thin-film solar cell must be thin enough to efficiently extract generated carriers, yet thick enough to effectively absorb incident light.

One method to increase the amount of light absorbed by these photovoltaic devices is the use of a thin-film dielectric antireflection coating (Figure 1.2). In this case, a thin dielectric layer with a certain thickness and refractive index is placed on top of the active material. As light passes from the incident medium into the coating layer, it is reflected at the interface between the coating and the incident medium and the interface between the coating and the active material. If the coating is of a certain thickness and refractive index then the reflected waves will destructively interfere and all of the light incident on the cell will be transmitted through the coating and into the active material. This helps ensure that all available light enters the cell, helping to mitigate the effects of the lack of optical thickness of many
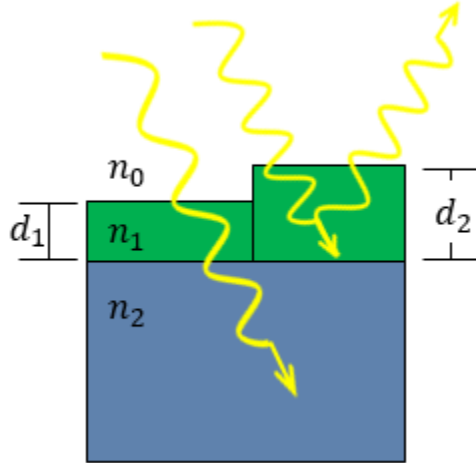
Figure 1.2: A simplified schematic of a thin-film dielectric antireflection coating. Light passes from a medium with refractive index n_0 into a properly designed coating of thickness d_1 and refractive index n_1. Upon reflection at the interface between the coating and the active material (refractive index n_2) the waves destructively interfere and all incident light is transmitted into the active material. This interference condition is valid for a coating with an index equal to $n_1 = \sqrt{n_0 n_2}$ and a thickness $d_1 = \frac{\lambda}{4n_1}$. For an improperly designed coating with thickness d_2 the reflected light will not destructively interfere and will therefore be reflected from the back surface of the coating.

thin-film solar cells.

Recently various concepts and designs have been utilized to raise the efficiency of thin-film photovoltaic cells beyond the enhancement provided by traditional thin-film dielectric antireflection coatings (ARCs). These ideas center around the field of nanophotonics. Nanophotonics describes the study of light at the nanoscale and its interactions with nanoscale objects. By fabricating nanoscale structures tailored to create certain responses from their interaction with incident light, possibilities such as coupling more light into the cell, inducing resonances at specific wavelengths, and angularly-independent absorption all become achievable. Some of these designs and

concepts include nano-textured transparent conducting oxides (TCOs) [1, 2], nanostructured dielectric reflectors [3–6], plasmonic structures [7–11], and more. The success and limitations of these strategies (including parasitic absorption and wavelength and angle sensitivity) only further emphasizes the need to take advantage of other optical mechanisms to increase absorption in thin-film solar cells.

1.2   III-V Materials and Nanostructuring

A recently proposed novel antireflection and photonic design concept was suggested using a periodic square array of subwavelength nanocylinders (NCs) on silicon [12]. These structures utilize Mie resonances, electromagnetic resonances that arise from the interaction of these structures with the incoming light. The Mie resonances couple to leaky optical modes in the high-index Si substrate, reducing the reflectance of the device to less than 8 % over the entire spectral range [12]. The resonances in the Si nanostructures have also been found to exhibit strong dependences on different geometric parameters such as nanocylinder diameter and array period [13]. Additional studies have shown that these types of nanostructures can be fabricated via inexpensive processes such as nanoimprint lithography, and exhibit significant light absorption enhancement in thin-film silicon solar cells [14, 15].

While these nanostructures and design techniques have yielded substantial improvements for Si, thin-film III-V photovoltaics with thicknesses $< 1\,\mu$m offer the possibility of even higher efficiencies. III-V materials, though expensive to manufacture, offer significant benefits such as radiatively limited recombination [16–18],

large absorption coefficients [19], high conversion efficiencies [20–22], and the possibility of built-in optical concentration [23]. The large absorption coefficients of direct bandgap III-V materials such as gallium arsenide (GaAs) and indium phosphide (InP) result in higher absorption using less material.

Thus, nanoscale optical coatings may result in similar performance enhancements using even thinner layers than can be achieved with Si-based devices; however, a potential disadvantage of nanostructuring is the possibility of increased non-radiative recombination processes [24, 25]. Because nanostructuring a material results in increased surface area and possibly substantial surface damage, the potential avenues for surface recombination to occur increase dramatically with surface nanostructuring. Though GaAs is the prototypical III-V photovoltaic material due to its ideal bandgap and high conversion efficiency, InP has the potential to perform similarly well and has a lower surface recombination velocity [26]. This quality makes InP an excellent candidate to explore nanostructured photovoltaic design concepts, and InP nanowire-based photovoltaic devices have already demonstrated great promise [27, 28]. In this work we have chosen to investigate the performance of nanostructured optical coatings on both GaAs and InP for the reasons outlined above.

1.3   Objectives and Goals

The primary goals and objectives of this thesis are to build off of the previous work done with Si nanocylinder coatings and extend those ideas to materials systems

ideally suited for nanostructuring and thin-film photovoltaics (InP and GaAs). We set out to perform three separate objectives:

- First, we want to fully optimize the design of these nanostructured coatings on both InP and GaAs by minimizing reflection from the device.

- Second, we want to identify the underlying physical mechanisms, which describe the performance of these structures.

- Third, we want to fully characterize the optoelectronic performance of these devices, including how these cells perform in a realistic, module-like design.

For reasons specified in Chapter 2, as each coating design is introduced, we will be focusing on a wide range of materials for the nanocylinder array coatings, consisting of the active photovoltaic material, titanium dioxide (TiO_2), and indium-tin-oxide (ITO). We aim to show that GaAs and InP solar cells with nanostructured coatings of these materials can outperform devices with traditional thin-film antireflection coatings through a combination of scattering resonances and thin-film interference effects. Further, we will demonstrate that these device can perform as well as devices with advanced multilayer ARCs, but without the need for multilayer coatings. Finally, we find that a nanostructured TiO_2 or ITO coating can further reduce reflection below that of a device consisting only of GaAs or InP, enabling a nanophotonic coating that does not affect the electronic properties of the underlying material.

1.4 Outline of Thesis

The current chapter, Chapter 1, has provided a brief introduction to the basic concepts covered in this thesis, as well as contextualized the motivation for the work.

Chapter 2 covers the design of the nanophotonic coatings and describes the optical simulations that form most of the backbone of the work in this thesis. First the software package and design methodology used will be outlined, followed by descriptions of the various coating designs and optical simulation results for each design. After summarizing the angularly-dependent reflection of a few selected coating designs, different results between the various coatings and active materials will be discussed.

Chapter 3 describes the methods, techniques, and results of investigating the optical mechanisms behind the performance enhancement provided by the nanophotonic coatings. Examinations of the electric field intensity profiles around individual nanostructures will be discussed in conjunction with studies of the optical modes of the structures. Both of these investigations reveal mechanisms which describe the enhancement.

Chapter 4 highlights the overall performance of the designed III-V solar cells with nanophotonic coatings as optoelectronic devices. First the electrical and device simulations are presented, which allow for the accurate determination of important solar cell parameters. Then optical results from simulating the cells in a module-like configuration and optical environment are discussed. In combination, these two studies characterize the optoelectronic performance of realistic devices utilizing our

nanostructured coatings.

Chapter 5 provides a conclusion for this thesis and presents opportunities for future work in this area. Additionally, Appendix A showcases a few extra figures and results of this work.

Chapter 2:   Coating Design and Optical Simulations

In this chapter, we will present the software and design methodology used to simulate and optimize various nanophotonic coating structures on InP and GaAs. We will describe each nanostructure, the context behind why the particular design was investigated, and summarize the results. However, it is important to note that the more thorough analysis of why we see these results will come in Chapter 3, once the optical mechanisms have been examined and explained. After this chapter, when referencing the nanocylinder coatings, we will be referencing the fully optimized geometries of these structures (*i.e.* the structures with the best optical performance). This chapter will describe the optimizations and optical results of the nanophotonic coatings investigated in this thesis.

2.1   Optical Modeling Software

To calculate the reflection and quantify the optical performance of these nanophotonic structures we perform three-dimensional finite-difference time-domain (FDTD) simulations using a commercially available software package (Lumerical FDTD Solutions). The FDTD method is a computational method used to solve Maxwell's equations for electromagnetic wave propagation in both time and space. Maxwell's

equations are solved on a discrete spatial and temporal grid, where each field component is solved at a slightly different location in each grid cell. This grid cell is called a "Yee cell", and its size is determined by the mesh size of the simulation, which can be manually or automatically set. The data is then interpolated to the origin of each grid point. Typically the finer the mesh the more computationally intensive and time consuming the simulation is, while too coarse of a mesh may yield inconclusive or unreliable results. The resulting solutions of the FDTD simulations can be converted into the frequency domain (thus in terms of the wavelength of the incident light) via Fourier transforms, which are implemented in the software package. Not only that, but certain boundary conditions can be specified to make sure the results are accurate. This provides a powerful tool to study the optical response of various coatings on active photovoltaic materials in a computational environment.

Setting up a simulation in Lumerical is fairly straightforward. The software provides a CAD-like environment and a GUI which can be used to add relevant objects to the simulation. Materials of specific geometries can be added and then adjusted as necessary, with the ability to specify the position, type of material, thickness, and other parameters of the object. A scripting language similar to MATLAB and C can be used to create periodic structures or specify an analysis to run after the simulation is complete. Lumerical also provides different options for sources of the electromagnetic radiation incident on the structure in the simulation, such as a dipole source or plane-wave source. The geometry, boundary conditions, and mesh size of the FDTD region itself can be specified, followed by the placement of various

monitors to measure the reflectance, absorption, or power flow at certain locations during the simulation. Finally, Lumerical contains a large database of optical data (*i.e.* real and imaginary refractive index data) for various materials which can be modified with user-inputted optical data as well. In order to successfully run these simulations, Lumerical fits the optical data to a polynomial used in the simulation with tolerances that can also be set by the user. This again provides a useful platform to customize the optical simulations and study specific structures or certain aspects of the optical responses of various materials and geometries.

2.2   Design Methodology

Because the main goal of these nanophotonic antireflection coatings is to minimize reflection and facilitate light in-coupling and absorption into the active photovoltaic material, we want to find the geometry of the nanocylinder array that minimizes the reflectance of the solar cell. To do this we use the following simulation guidelines. The structure is illuminated with p-polarized normally incident light from a broadband plane-wave optical source, corresponding to the above bandgap components of the solar spectrum for InP (λ = 350 nm to 925 nm) and GaAs (λ = 350 nm to 871 nm). We use 350 nm as our starting wavelength for reasons described later in this section. A reflection monitor is placed above the optical source to measure the total amount of light reflected from the device. For all of our simulations, we assume ambient room temperature conditions (T = 300K), which we used to obtain our values for the cutoff wavelength for InP and GaAs [29]. The cutoff

13

wavelength for a semiconductor is the wavelength corresponding to the energy of the semiconductor's bandgap, indicating the wavelength beyond which no light is absorbed.

We define a simulation region based on the specific geometry of the nanocylinders (periodicity and height). A single unit cell is simulated, with periodic boundary conditions to replicate the periodic square array of nanocylinders. The simulation region also penetrates 100 nm into the active material layer, though we use a perfectly matched layer (PML) boundary condition at the bottom of the simulation volume to simulate an infinitely thick layer of InP or GaAs. This allows us to study only the coupling of the incident light into the active material without additional effects due to light reflection off the back surface. Simulations of finite thickness samples in a device-like architecture are discussed in Chapter 4.

Periodic hexagonal arrays of these structures were also investigated, but the results had negligible deviations from the square array results, leading us to focus on square arrays for simplicity. In all of the simulations, the mesh size was refined until there was negligible change in the reflectance spectrum, typically less than a few hundredths of a percent (corresponding to mesh sizes on the order of 1 nm). Wavelength-dependent optical data (n,k) was obtained from [19] for InP and GaAs, [30] for TiO_2, and Lumerical's materials database for ITO. Over the relevant spectral ranges ($\lambda = 350$ nm to 871 or 925 nm), the real part of the refractive index is ~3.7 for InP and GaAs, ~1.8 for ITO, and ~2.5 for TiO_2.

Now that we have set up the framework of our reflectance simulations, we determine the optimal geometries for these nanostructures, namely geometries which
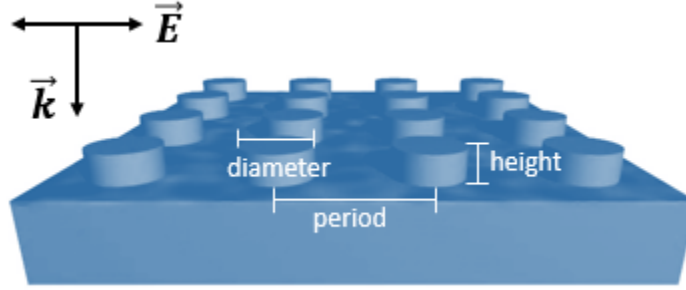
Figure 2.1: A diagram of an array of active material nanocylinders, highlighting the three geometric parameters of the nanocylinders that were varied during the optimization and design process. This general geometry is consistent between all nanostructured coatings investigated in this thesis.

minimize the reflectance of the photovoltaic device. The three adjustable geometric parameters of the nanocylinder arrays - diameter, period, and height - are indicated in Figure 2.1. To cover a wide range of potential geometries and designs we perform large parameter sweeps of the nanocylinder diameter and period for four specific nanocylinder heights (50 nm, 100 nm, 150 nm, and 200 nm). However, optimizing these structures via minimized spectral reflectivity fails to consider the spectral characteristics of the incident radiation (*i.e.* the solar spectrum), because we use a simple plane wave source for these simulations. As a result, we must devise a new figure of merit to use for these geometric optimizations which considers the reflectance of the devices, as well as the photon flux and spectral characteristics of the real solar spectrum.

To address this issue, we utilize a solar-weighted reflectivity ($R_{AM1.5G}$). We weight the reflectance from the device by the actual spectral photon flux (photons per unit time per unit area per wavelength) from incident sunlight in order to

15

determine the fraction of photons that are reflected from the device under solar illumination. The incident spectral photon flux from the sun is a quantity determined by NREL and subject to standards set by the solar industry. In calculations of efficiency for non-concentrating solar cells it is standard to use the AM1.5G (Global) spectrum, while AM1.5D (Direct) is used for concentrating photovoltaics. The spectrum is simply measured data of the incident power (which can be converted to a photon flux) of solar radiation on Earth averaged over the year and for generic atmospheric conditions. We calculate the solar-weighted reflectivity using the spectrally resolved reflectivity from the nanostructured solar cell, $R(\lambda)$, weighted by the solar photon flux from the AM1.5G spectrum at each wavelength, $\phi_{AM1.5G}(\lambda)$, which is integrated over the available wavelengths ($\lambda_{min} = 350$ nm to $\lambda_g = 871$ nm or 925 nm, the bandgap wavelength of the active photovoltaic material):

$$R_{AM1.5G} = \frac{\int_{\lambda_{min}}^{\lambda_g} R(\lambda)\phi_{AM1.5G}(\lambda)d\lambda}{\int_{\lambda_{min}}^{\lambda_g} \phi_{AM1.5G}(\lambda)d\lambda}. \tag{2.1}$$

We use 350 nm as a starting wavelength for all of our simulations because only 2% of the total power density in the AM1.5G solar spectrum for wavelenghts < 1 μm is present for wavelengths below 350 nm. Using this figure of merit (Equation 2.1), we obtain the solar-weighted reflectance as a function of nanocylinder geometry, and find the optimal geometry for the nanocylinders by finding which geometry minimizes the solar-weighted reflectance.

2.3   Active Material Nanocylinder Coating

The first type of nanostructured coating we examined was a coating consisting of nanocylinder arrays of the active photovoltaic material, either InP or GaAs. We performed optical simulations following the process outlined in the previous section and performed vast sweeps of the geometric parameter space to find the optimal NC geometry which minimized the $R_{AM1.5G}$. We performed these optimizations for four NC heights from 50 nm to 200 nm in 50 nm intervals, for NC diameters from 20 nm - 400 nm in 20 nm intervals (depending on the NC height), and for NC array periods from 20 nm - 700 nm also in 20 nm intervals (depending on the NC height). For each individual simulation we extracted the spectrally resolved reflectance and the solar-weighted reflectivity. We then plotted the solar-weighted reflectance as a function of NC period and diameter on a contour plot and found the minimum to determine the optimized geometry.   The results of our optimizations for both InP nanocylinders and GaAs nanocylinders are shown in Figure 2.2 (a) and (b). Both plots only show the results for h = 100 nm NCs because NCs at that height had the lowest solar-weighted reflectance for all of the NC heights we examined. Results for the optimizations we performed for the other three NC heights are presented in Appendix A.

For both InP and GaAs, the NCs which minimized the solar-weighted reflectance from the cell had the same geometric dimensions: a height of 100 nm, diameter of 120 nm, and array period of 180 nm. This optimized geometry is indicated by the black diamonds in Figure 2.2. In these optimizations we used a
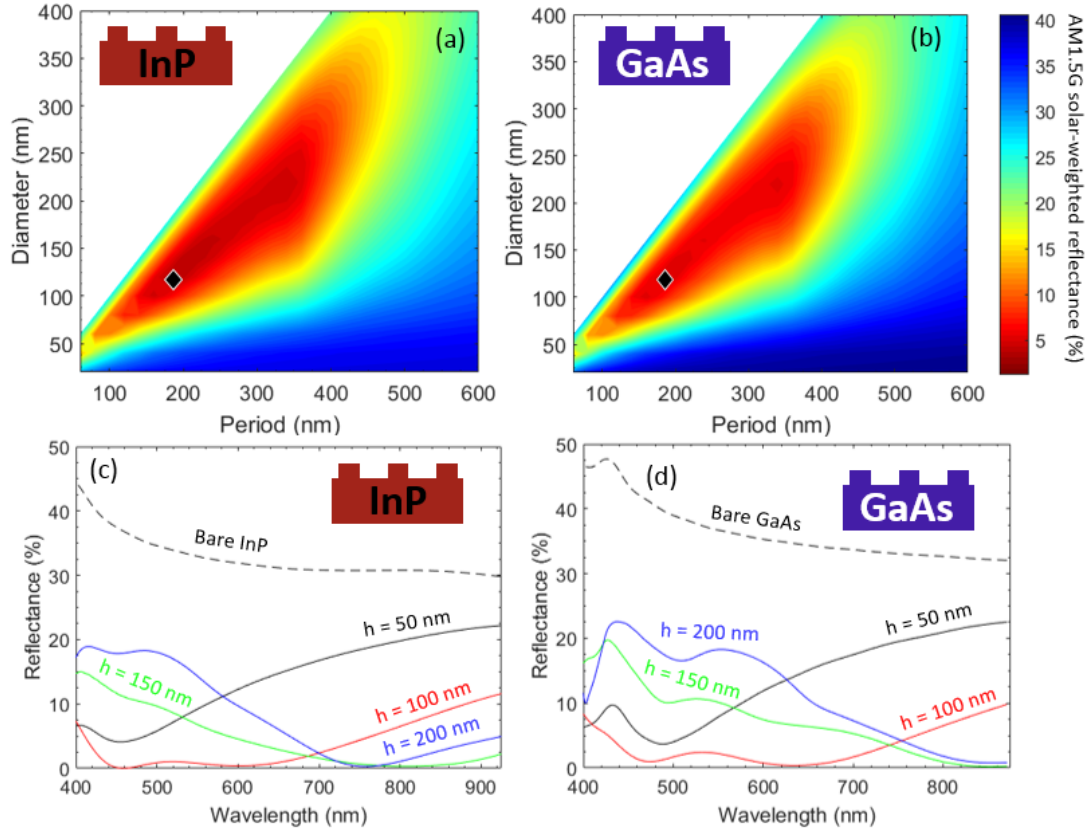
Figure 2.2: Solar-weighted reflectivity and spectrally resolved reflectance for InP and GaAs nanocylinder coatings. (a) Contour map of the solar-weighted reflectivity of nanocylinder coatings in InP as a function of NC diameter and period. (b) Same as (a) but for NCs in GaAs. Both (a) and (b) show results for NCs with a height, $h = 100$ nm, with the optimized geometry indicated by the black diamond. (c) Spectrally resolved reflectance for optimized NC active material coatings of various geometries in InP: bare InP substrate (black dashed line), $h = 50$ nm NCs (black), $h = 100$ nm NCs (red), $h = 150$ nm NCs (green), and $h = 200$ nm NCs (blue). (d) Same as (c) but for GaAs.

color-scale which emphasized the low reflectance regions in red and the high re-flectance regions in blue. It is interesting to note that there is a clear peak region in the contour plot and that at larger periodicities, the solar-weighted reflectance of the active material nanocylinders seems to drop off. This drop off is likely a result of

reduced nanocylinder-to-nanocylinder coupling, which decreases as the nanocylinders are moved further and further apart.

Figure 2.2 (c) and (d) present the spectrally resolved reflectances of the bare substrates and of the optimized nanocylinders for each height. Clearly the nanocylinder arrays made of active material drastically reduce the overall reflection of the device compared to the bare substrate. It is also interesting that the intermediate height ranges (100 nm and 150 nm) produce NC array geometries that further reduce the reflectance over a large spectral range. In particular, the red curve representing the 100 nm NCs shows broad dips in the reflectance over almost the entire visible range (400 nm - 700 nm), exhibiting the potential of these active material NC coatings as a method of enhanced antireflection. We can take these spectrally resolved reflectances and convert them directly to solar-weighted reflectances via Equation 2.1, which yields the results of Table 2.1. As we shall show later in this thesis, these $R_{AM1.5G}$ values demonstrate a nearly 90 % reduction in solar-weighted reflectance compared to a bare substrate, again showcasing the potential of these types of coatings.

Table 2.1: Solar-weighted reflectivity ($R_{AM1.5G}$) for all optimized active material nanocylinders. The results are shown for each of the four nanocylinder heights that were investigated.

	$R_{AM1.5G}$ for various NC heights			
Substrate Material	h = 50 nm	h = 100 nm	h = 150 nm	h = 200 nm
InP	8.06 %	3.68 %	8.49 %	14.08 %
GaAs	7.70 %	4.72 %	11.36 %	17.46 %

2.4   Titanium Dioxide Nanocylinder Coating

Even though InP and GaAs have relatively low surface recombination velocities, nanostructuring may still increase recombination. To avoid potential performance degradations resulting from a textured active layer, we explored the use of nanostructured TiO_2 coatings on these III-V solar cells as a means to maintain similar optical enhancement without negatively impacting the overall device performance.

2.4.1   Advantages of Titanium Dioxide

TiO_2 might not be a material that typically comes to mind when one conceives of an optical coating material for a solar cell due to its high refractive index. However, it has been shown that TiO_2 is a highly effective passivating layer when used as a coating on InP [31], may be used as a highly efficient hole-selective contact [32], and provides substantial optical improvement when used as a nanostructured coating on Si [33]. This body of work has laid the groundwork for these types of coatings, though they have not been extensively studied for use as antireflection coatings on III-V solar cells. The TiO_2 nanostructured coatings we have designed include a thin TiO_2 spacer layer separating the nanocylinders from the InP active layer, which would aid with surface passivation and improved optical performance in a fabricated device. To determine the thickness of the spacer layer, we perform sweeps similar to those made with the active material nanostructures. For these simulations we swept the thickness of the TiO_2 spacer layer with and without an addditional NC coating
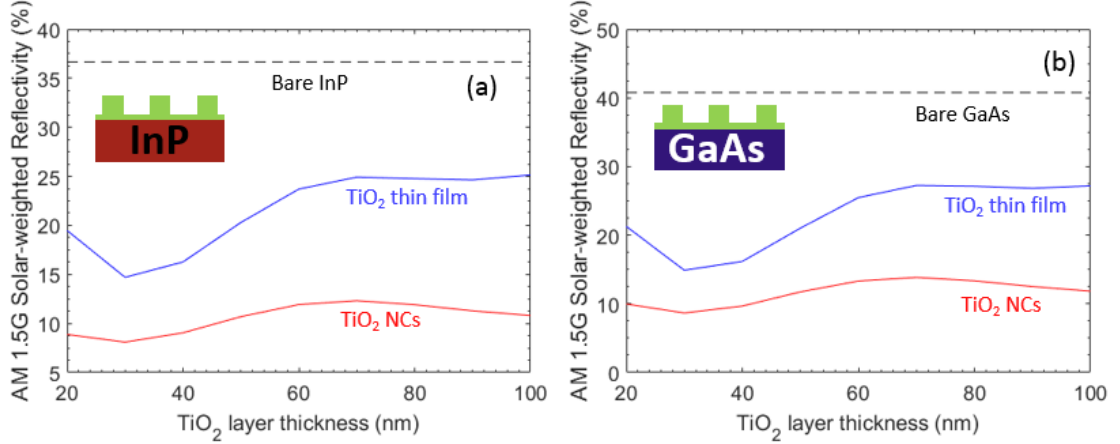
Figure 2.3: Solar-weighted reflectivity of TiO_2 coatings on (a) InP and (b) GaAs for varying thicknesses of the TiO_2 spacer layer. For (a) and (b) the black dashed line indicates the $R_{AM1.5G}$ of the bare substrate material, the blue line represents the TiO_2 film with no NC coating on top, and the red line represents a generic NC coating ($h = 100$ nm, $p = 500$ nm, $d = 350$ nm). The results for the NC coating do not vary significantly with different NC geometries.

instead of sweeping the NC geometric parameters. The results of these thickness sweeps for a TiO_2 layer on both InP and GaAs are shown in Figure 2.3. From these results, we determined that a 30 nm thick spacer layer provides the lowest solar-weighted reflectance over the full spectral range regardless of nanocylinder geometry.

2.4.2   Nanostructure Optimization and Results

We then perform optimizations mirroring those from section 2.3 for the active material nanocylinder coatings, this time using our TiO_2 NC coatings with a 30 nm thick TiO_2 spacer layer. The results of these geometry optimizations are shown in Figure 2.4. These optimizations revealed that TiO_2 nanocylinders with a

Figure 2.4: Solar-weighted reflectivity and spectrally resolved reflectance for TiO_2 nanocylinder coatings on InP and GaAs. (a) Contour map of the solar-weighted reflectivity of TiO_2 nanocylinder coatings on InP as a function of NC diameter and period. (b) Same as (a) but for NCs in GaAs. Both (a) and (b) show results for NCs with a height, $h = 100$ nm, with the optimized geometry indicated by the black diamond. (c) Spectrally resolved reflectance for optimized TiO_2 NC coatings of various geometries in InP: bare InP substrate (black dashed line), $h = 50$ nm NCs (black), $h = 100$ nm NCs (red), $h = 150$ nm NCs (green), and $h = 200$ nm NCs (blue). (d) Same as (c) but for GaAs.

height of 100 nm, diameter of 180 nm, and array period of 320 nm minimize the

solar-weighted reflectance from both InP and GaAs substrates. While the overall

results are qualitatively similar to the contour plots from Figure 2.2, the quantita-

tive range of solar-weighted reflectances covered by these structures is about half of

those covered by the active material NCs (from 3 % - 40 % to 2 % - 20 %). This is evidence that the TiO_2 NCs have much lower solar-weighted reflectances across the entire parameter space, as can be seen in (a) and (b) of Figure 2.4.

Again, we can gain further insight by examining the spectrally resolved reflectances of the optimized TiO_2 NCs for each NC height, as seen in (c) and (d) of Figure 2.4. For the $h = 50$ nm NCs on both substrate materials (indicated by the black solid lines), the spectrally resolved reflectance looks similar to that of a single layer antireflection coating. A possible explanation for this effect will be provided in the next chapter when the optical mechanisms are discussed. The optimized structures ($h = 100$ nm, red solid lines) yet again show large, broad reflectance dips throughout the visible spectrum. The results of converting these reflectances into solar-weighted reflectivities are shown in Table 2.2. These solar-weighted reflectivities are significantly lower than those of the active material NCs, supporting the choice of TiO_2 as a nanostructured antireflection coating material for III-V solar cells.

To further validate the effect of the TiO_2 NCs and TiO_2 spacer layer as an

Table 2.2: Solar-weighted reflectivity ($R_{AM1.5G}$) for all optimized TiO_2 nanocylinders. The results are shown for each of the four nanocylinder heights that were investigated.

	$R_{AM1.5G}$ for various NC heights			
Substrate Material	h = 50 nm	h = 100 nm	h = 150 nm	h = 200 nm
InP	5.67 %	1.25 %	3.62 %	6.57 %
GaAs	6.23 %	1.23 %	4.08 %	6.87 %

antireflection coating structure, we modified our simulations slightly in order to determine the absorption in the TiO_2 NC coating and the active photovoltaic layer directly. By determining the absorption in the TiO_2 layers, we could confirm that the coatings are working as intended, not simply absorbing a large fraction of the incident light as their main contribution to lowering the solar-weighted reflectivity of the structure. The goal of these structures is to aid in-coupling of light to the solar cell rather than acting as an additional absorbing medium. We modified our optical simulations to measure this absorption by including two new reflectance monitors, one at the interface between the TiO_2 spacer layer and the active material and another at the interface between air and the top of the NC array. By calculating the difference in power transmitted from the top monitor to the bottom monitor, we could directly determine the power absorbed in both the coating and the substrate. This is possible because we are assuming that all light that is transmitted into the substrate is eventually absorbed, which is a good approximation because we are using a semi-infinite substrate due to the PML boundary condition at the bottom of the FDTD simulation region.

The results of these simulations for the optimized TiO_2 NC geometries are shown in Figure 2.5. Though the overall absorption in the TiO_2 layer is minimal in comparison to that in the substrate, it is certainly not negligible, especially at shorter wavelengths. This makes sense, however, as shorter wavelength light is more likely to be absorbed closer to the surface of a material because it has a small penetration depth. Additionally, TiO_2 has an extinction coefficient (and therefore absorption coefficient) that is much higher at wavelengths below 400 nm, making

Figure 2.5: Spectrally resolved layer-by-layer absorption for optimized TiO$_2$ NCs on (a) InP and (b) GaAs. In (a) and (b) the blue region represents the absorption in the substrate while the red region represents the absorption in the TiO$_2$ coating layer.

it more likely to absorb light at those wavelengths. To put the absorption in these layers into the proper context, namely potential optical performance for device operation, we can use Equation 2.1 and substitute the spectrally resolved reflectivity $R(\lambda)$ for the spectrally resolved absorptivity $A(\lambda)$ to calculate the solar-weighted absorptivity ($A_{AM1.5G}$) in each layer. For the overall structure, we can simply use the following relation to calculate the solar-weighted absorptivity (as a percentage), because all incident light is either absorbed or reflected in these simulations:

$A_{AM1.5G} = 100 - R_{AM1.5G}$.

We can see quantitatively from Table 2.3 that the absorption in the TiO$_2$ layer for both InP and GaAs makes up almost 10 % of the total absorbed power from the device. While this is fairly significant, 90 % of the total absorbed light being transmitted into the substrate, along with the enhanced antireflection effects at the front

surface, is further validation of this type of coating design. While other coatings may absorb less incident light, it is difficult to compete with ~1.25 % solar-weighted reflectivity across the relevant spectrum.

Table 2.3: Solar-weighted absorptivity ($A_{AM1.5G}$) in each layer for optimized TiO_2 nanocylinder coatings on InP and GaAs.

	$A_{AM1.5G}$		
Substrate Material	Total $A_{AM1.5G}$	In substrate	In TiO_2
InP	98.75 %	91.03 %	7.70 %
GaAs	98.77 %	89.92 %	8.82 %

2.5 Fabrication Considerations - ITO Nanocylinders

While these optical investigations are interesting and reveal insights into these kinds of nanostructured coating designs on III-V photovoltaic materials, the end goal of this research is to fabricate and test these coatings, ideally building towards making them viable alternatives to typical antireflection coatings. When examining different fabrication processes for creating these nanostructured coatings, the facilities available in the UMD Nanocenter and AIM Lab immediately came to mind. The new FIB/SEM system provides an opportunity for nanopatterning to create the structures and high quality imaging in-situ. However, some of the issues with FIB patterning resulted in us investigating another potential coating material.

2.5.1 Focused Ion Beam and Charging Problems

Focused ion beam (FIB) is a microscopy technology which uses ions instead of electrons (such as those used in SEM, scanning electron microscopy) for imaging and patterning purposes. The FIB/SEM systems at UMD use either Gallium or Xenon (Xe) ions, though the Xe ions are much larger and are therefore used for larger-scale imaging and patterning. Because our structures are on the order of hundreds of nanometers, we would want to use the Ga system for our nanopatterning. This patterning works essentially by material ablation, as high energy Ga ions are focused into a beam which blasts away material from the sample. Images in the FIB can be acquired through secondary ions that are scattered from the beam's interaction with the sample, or more typically, secondary electrons. Scattered secondary electrons are also the primary imaging method for the SEM.

However, Ga ions are positively charged, so the ion beam acts as a large beam of positive charge hitting the sample. Over time the exposure of the surface to the beam can cause the sample to develop a net positive charge. As a result of this charging, emitted secondary electrons (negatively charged) will be attracted back towards the surface of the sample and thus not be collected for imaging purposes. This causes the image of the sample to look black due to the lack of secondary electrons reaching the detector in the FIB system. Not only that, but excess sample charging can result in improper nanopatterning or milling of the sample. In order to mitigate this charging effect conductive coatings are typically deposited on the sample to facilitate charge movement away from the sample and towards the

grounded sample holder. In our experiment, we want to deposit a non-conductive dielectric coating on top of our solar cells to pattern into nanocylinder arrays, so having a conductive coating on top of the dielectric coating seemed counterintuitive. Upon further thought, it would be interesting to see how a transparent conductive coating, a type of material often used in solar cell design and development, would work as a nanostructured antireflection coating.

2.5.2 ITO Nanocylinders

This realization lead us to use Indium Tin Oxide (ITO) as another potential coating material for our III-V photovoltaic devices. ITO is a transparent conducting oxide (TCO) used in various optoelectronic applications, including solar cells. Using ITO as the material for our nanocylinders would alleviate the charging problem of FIB fabrication and potentially increase the effectiveness of these structures as antireflection coatings. Not only that, but with an index of ~ 1.8 over the visible spectrum, ITO has optical properties that are close to optimal for a single layer antireflection coating on InP or GaAs, using the relation described in Figure 1.2. We perform the same simulations described in the previous section to determine the thickness of an ITO spacer layer between the nanocylinders and the active photovoltaic material. The results are shown in Figure 2.6 below. From these results, we determined that a 50 nm spacer layer would minimize the solar-weighted reflectance from the device. Though using the NCs decreased this optimal thickness to 40 nm, we went with the 50 nm from the thin-film simulations for reasons which will be

described in Chapter 3.

Once we had determined the optimal spacer layer thickness we again performed sweeps of the parameter space to find the geometries of the ITO NC arrays which would minimize the solar-weighted reflectance from the devices. We can see from the results, shown in Figure 2.7, that the optimized geometries for the ITO NCs are fairly similar to those of the TiO$_2$ NCs. For InP the optimized NCs had a height = 100 nm, a diameter of 180 nm, and an array period of 340 nm, while for GaAs the larger NCs with a height of 150 nm, a diameter of 200 nm, and an array period of 360 nm minimized the solar-weighted reflectance. Though the range of $R_{AM1.5G}$ in these sweeps has a higher minimum than the TiO$_2$ NCs, the magnitude of $R_{AM1.5G}$ across all of the geometries simulated is much lower on average than the TiO$_2$ NCs.
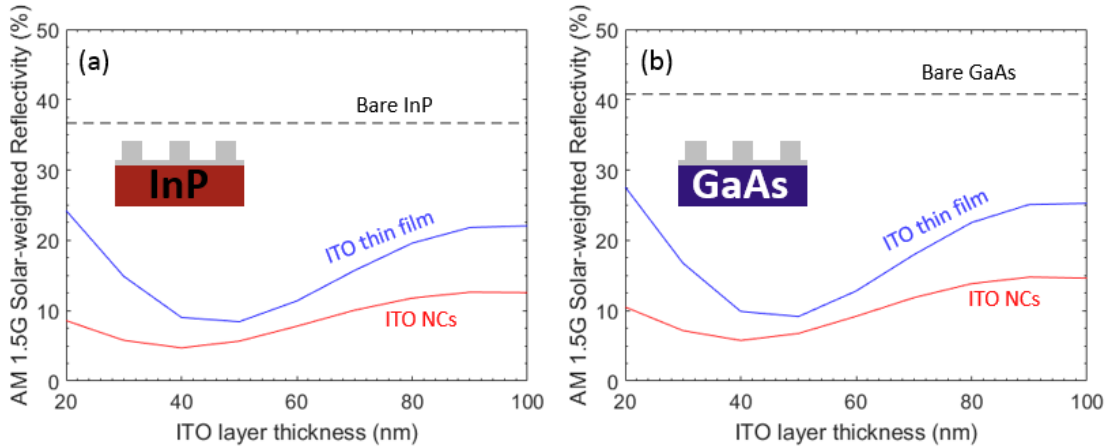
Figure 2.6: Solar-weighted reflectivity of ITO coatings on (a) InP and (b) GaAs for varying thicknesses of the ITO spacer layer. For (a) and (b) the black dashed line indicates the $R_{AM1.5G}$ of the bare substrate material, the blue line represents the ITO film with no NC coating on top, and the red line represents a generic NC coating ($h = 100$ nm, $p = 500$ nm, $d = 350$ nm). The results for the NC coating do not vary significantly with different NC geometries.
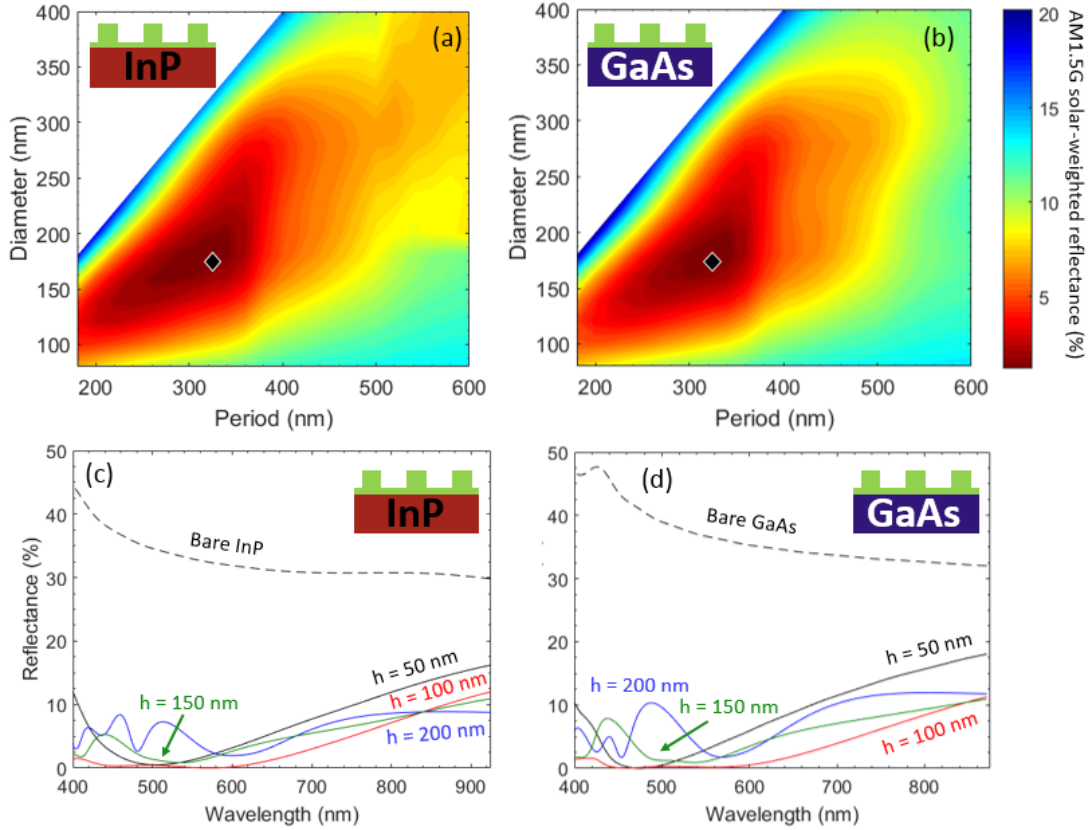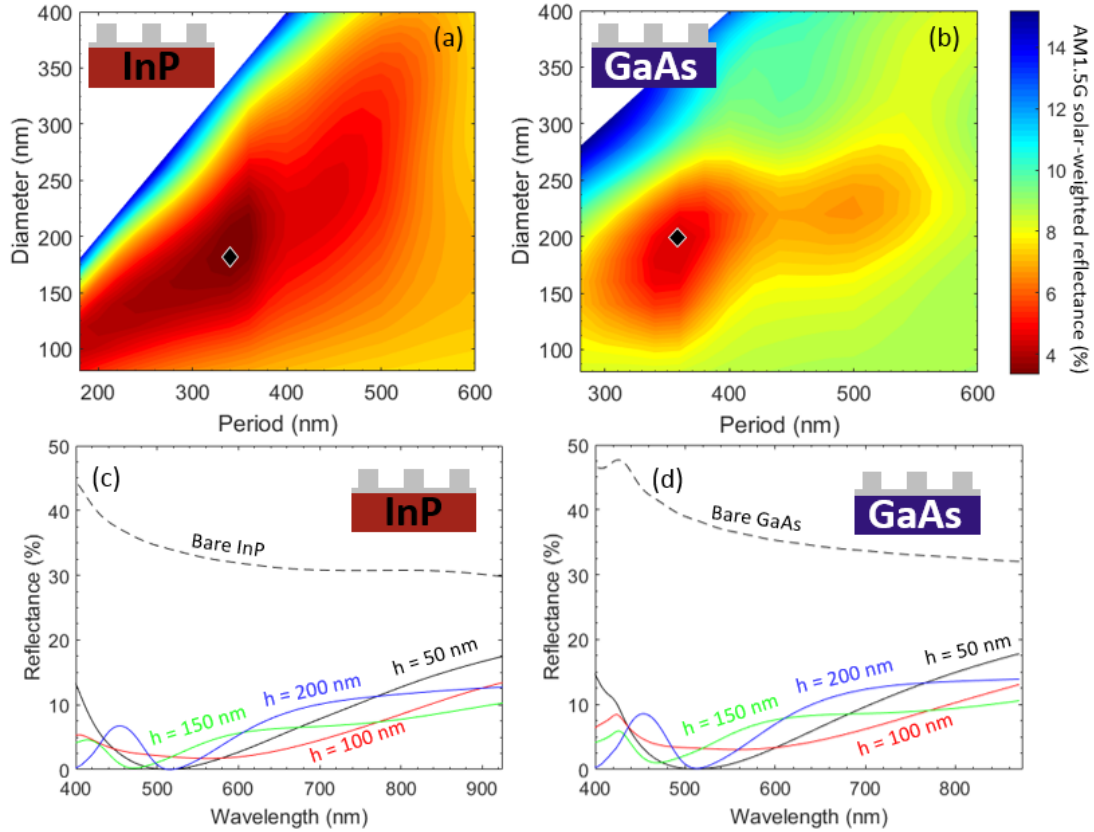
Figure 2.7: Solar-weighted reflectivity and spectrally resolved reflectance for ITO nanocylinder coatings on InP and GaAs. (a) Contour map of the solar-weighted reflectivity of ITO nanocylinder coatings on InP as a function of NC diameter and period for a NC height of 100 nm. (b) Same as (a) but for NCs with a height of 150 nm on GaAs. Both (a) and (b) indicate the optimized geometry by a black diamond. (c) Spectrally resolved reflectance for optimized ITO NC coatings of various geometries in InP: bare InP substrate (black dashed line), $h = 50$ nm NCs (black), $h = 100$ nm NCs (red), $h = 150$ nm NCs (green), and $h = 200$ nm NCs (blue). (d) Same as (c) but for GaAs.

We can see through the spectrally resolved reflectance plots in (c) and (d) of Figure 2.7 that these structures maintain the broad reflectivity drops characteristic of the previous coating structures we have examined.

Converting these spectrally resolved reflectivities to solar-weighted reflectivi-

Table 2.4: Solar-weighted reflectivity ($R_{AM1.5G}$) for all optimized ITO nanocylinders. The results are shown for each of the four nanocylinder heights that were investigated.

	$R_{AM1.5G}$ for various NC heights			
Substrate Material	h = 50 nm	h = 100 nm	h = 150 nm	h = 200 nm
InP	6.96 %	3.34 %	3.60 %	5.04 %
GaAs	8.17 %	4.54 %	4.45 %	5.61 %

ties via Equation 2.1 yields the results in Table 2.4. We can see that these results are consistent with results for previous NC coatings, where the intermediate NC heights have minimized $R_{AM1.5G}$ while the more extreme structures have decreased optical performance. These values fall in between those from the active material NCs and the TiO$_2$ NCs, indicating that using this transparent conductive layer as a nanostructured coating still provides a benefit over nanostructuring the active photovoltaic material. This provides good incentive for us to fabricate these structures as opposed to others, in order to alleviate charging problems that might arise with processing in the FIB.

This perception of the ITO coatings changes, however, when we take a closer look at the absorption in the ITO layer. The ITO absorbs much more incident light than TiO$_2$ and is more consistent in its absorption across the entire spectrum (Figure 2.8). While the strong absorption at short wavelengths is still present due to the reasons outlined in the previous section regarding short-wavelength incident light, the continued strong absorption throughout the spectrum is a negative aspect of using ITO as a NC coating material. This absorption detracts from potential pho-

ton absorption and resulting carrier generation in the active photovoltaic material substrate, thereby decreasing the potential efficiency increase the nanostructured coating could provide.

The negative aspects of this parasitic absorption in the ITO layer are made more apparent by calculations of the solar-weighted absorptivity in each layer, as outlined in Section 2.4. Looking at the results in Table 2.5, we can see quantitatively the massive increase in absorption in the ITO layer compared to TiO_2 from the previous section (Table 2.5). Almost 15 % of the incident light absorbed by the device is absorbed in the ITO layer. This drastically diminishes the amount absorbed in the substrate and made available for generating electron-hole pairs and thus usable electric current. This calculation provides a good check on the optical results we calculated from the solar-weighted reflectivity of the overall structure,
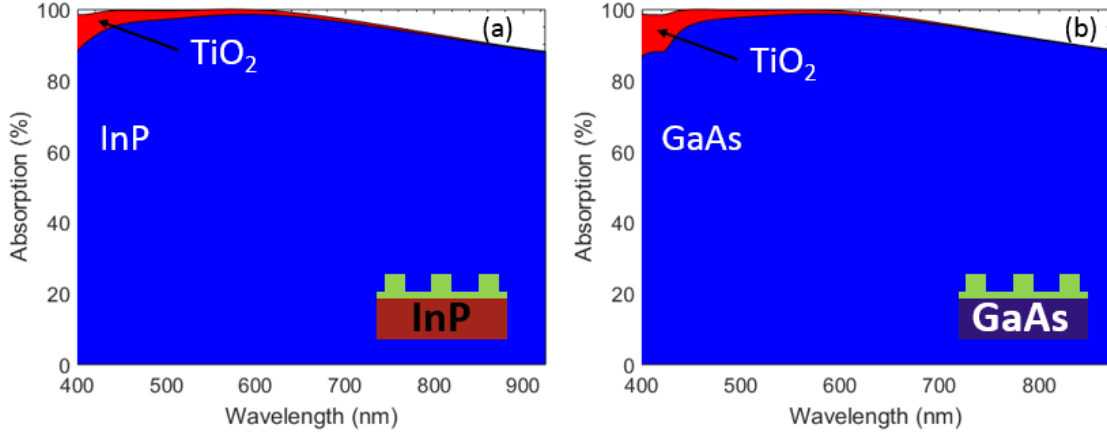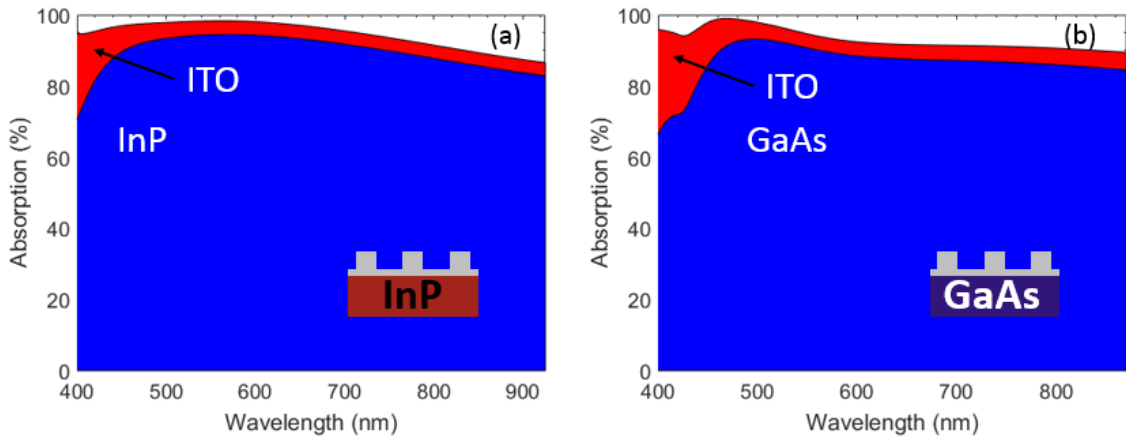

Figure 2.8: Spectrally resolved layer-by-layer absorption for optimized ITO NCs on (a) InP and (b) GaAs. In (a) and (b) the blue region represents the absorption in the substrate while the red region represents the absorption in the ITO coating layer.

and provides another metric by which we can gauge the overall optical performance of these nanostructured coatings.

Table 2.5: Solar-weighted absorptivity ($A_{AM1.5G}$) in each layer for optimized ITO nanocylinders on InP and GaAs.

	$A_{AM1.5G}$		
Substrate Material	Total $A_{AM1.5G}$	In substrate	In ITO
InP	96.66 %	83.12 %	13.42 %
GaAs	95.55 %	77.24 %	18.22 %

2.6 Antireflection Coatings

In order to determine how our nanostructured coatings compare with the current state-of-the-art optical designs for solar cells, we performed simulations of various antireflection coatings on InP and GaAs. These calculations provided us with a baseline of data to compare with the results for our nanostructured coatings and gave context to our designs with respect to current optical techniques.

2.6.1 Current Materials and Design Schemes

As described in Chapter 1, thin-film dielectric antireflection coatings have been implemented in photovoltaic design to reduce reflection at the front surface of the cell and facilitate light in-coupling for absorption and the generation of electron-hole pairs. These coatings achieve these goals through a thin-film interference effect, where a coating of the proper thickness and refractive index causes destructive

interference in the film and no reflected light for a specific wavelength. Two typical materials for these single layer antireflection coatings are Silicon Nitride (Si_3N_4) and Magnesium Fluoride (MgF_2). Magnesium fluoride can be used as a simple single layer ARC on some photovoltaic devices and is used as the top layer of the dual layer ARC on the InP solar cell with the world record power conversion efficiency [22]. Silicon nitride, on the other hand, is probably the most widely used single layer ARC, because it is the primary ARC material for Si solar cells and has an index of ~ 2.1 over the visible spectrum. This index is close to the optimized index of a single layer ARC on InP or GaAs of ~ 1.9, making Si_3N_4 a great candidate material to test our nanostructured ARCs against. We also chose to examine a TiO_2 single layer ARC, to see how TiO_2 performed as an ARC on its own without nanostructuring.

Single layer antireflection coatings are not the only optical design method to reduce reflection. In the highest-efficiency photovoltaic devices a dual layer ARC is used, with a top and bottom layer optimized to facilitate more light in-coupling into the cell at a broader range of wavelengths. For example, the InP solar cell with the world record power conversion efficiency used a dual layer ARC made up of a bottom layer of Zinc Sulfide (ZnS) and a top layer of MgF_2 [22]. By comparing the performance of our nanostructured coatings to this dual layer ARC, we can evaluate their optical performance with that of the proven technology in the field. While there are many other potential avenues for optical design, such as those discussed in the introduction (nanostructured TCOs, plasmonic nanostructures, etc.), we chose to focus on dielectric-based ARCs in order to compare our designs with the most widely developed, implemented, and proven technology. The goal of these simulations was

to provide accurate context of how our designs performed optically when compared to simpler and more widespread optical coatings for photovoltaics.

2.6.2 Optimizations and Results

Before we could compare the optical performance of our coatings with those of single and dual layer ARCS, we needed to determine the optimal thicknesses of these ARCs on InP and GaAs. We used the same methods for determining the spacer layer thicknesses for TiO_2 and ITO to determine the thicknesses of the ARCs, summarized by the results shown in Figure 2.9 for Si_3N_4. From these results we can see that the optimized thickness of a single layer Si_3N_4 ARC on InP or GaAs is 50 nm. We already determined the optimal spacer layer thickness for TiO_2 on InP and GaAs, 30 nm, and through the same simulations found an 80 nm ARC of MgF_2 also minimized $R_{AM1.5G}$ from the devices. For the dual layer ARC we needed to perform thickness sweeps, similar to the geometry sweeps we ran on the nanocylinder coatings, to determine the thicknesses of both the top and bottom layer of the ARC simultaneously which minimize the solar-weighted reflectance of the device. These thickness sweeps revealed that a dual layer ARC with 40 nm of ZnS and 90 nm (InP) or 80 nm (GaAs) of MgF_2 formed the optimal dual layer coatings for their respective photovoltaic materials (Figure 2.9).

As with previous coatings, we can gain further insight by examining the spectrally resolved reflectance. We can see from Figure 2.10 that the dual layer ARC has the lowest reflectance across the entire spectrum, as expected. Addition-
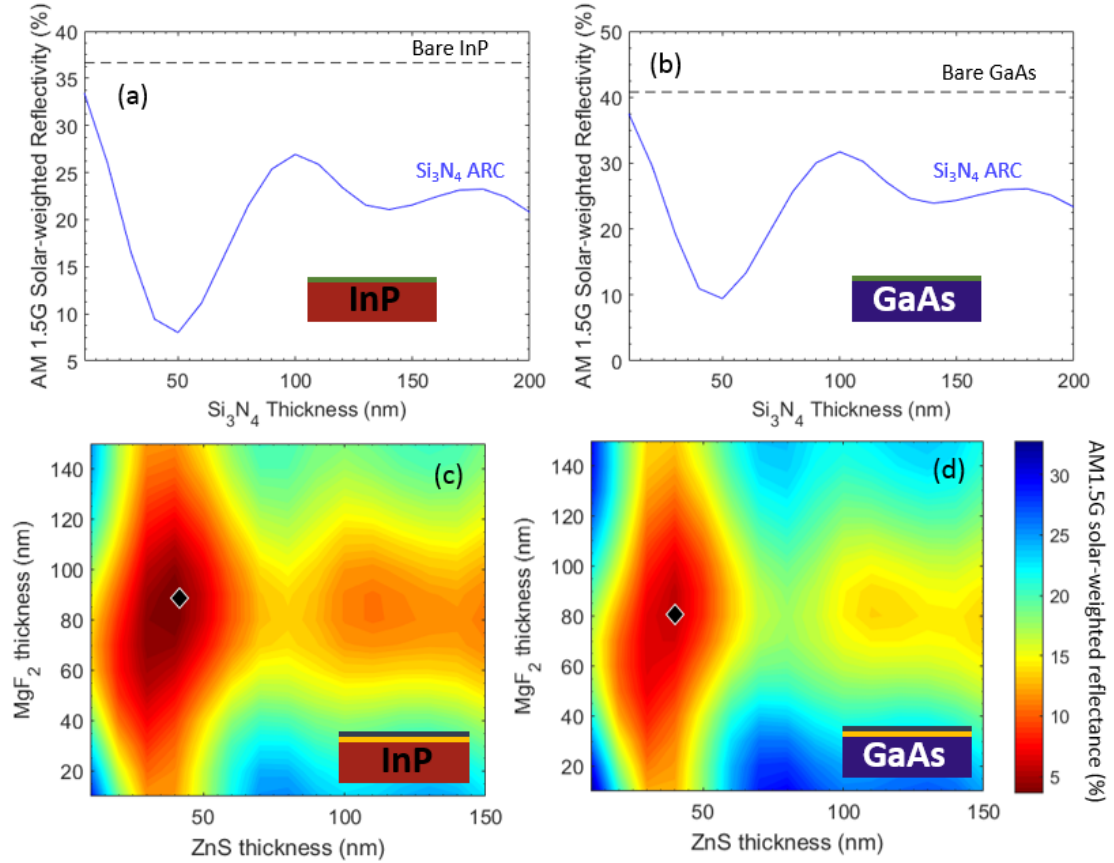
Figure 2.9: Solar-weighted reflectivity of a single layer (a,b) and a dual layer (c,d) ARC on (a,c) InP and (b,d) GaAs for varying thicknesses of the coating layers. For (a) and (b) the black dashed line indicates the $R_{AM1.5G}$ of the bare substrate material and the blue line represents the device with the coating, in this case Si_3N_4. (c) and (d) show contour plots of the $R_{AM1.5G}$ for varying the thickness of each layer in a dual layer ZnS and MgF_2 coating on (c) InP and (d) GaAs. The black diamond indicates the thicknesses of each layer for the optimized dual layer coating.

ally, we can clearly see the differences between a single and dual layer ARC in these reflectance plots. The reflectance of the Si_3N_4 ARC is minimized for a particular wavelength, around 450 nm, and then gradually increases for longer wavelengths of light. The minimized reflectance region is quite small and narrow, while for the dual layer ARC the region of minimized reflectance is quite broad and covers almost the
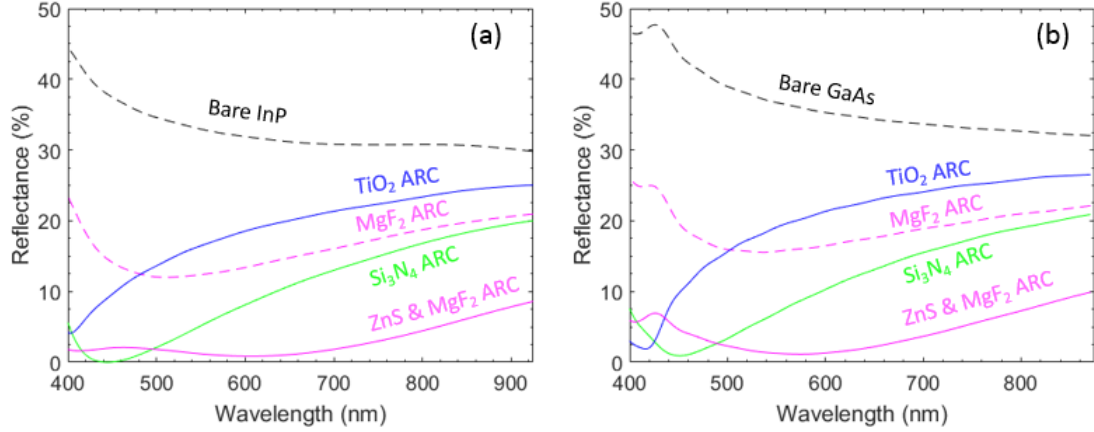
Figure 2.10: Spectrally resolved reflectance for various single and dual layer ARCs on (a) InP and (b) GaAs: bare substrate (black dashed line), MgF$_2$ ARC (magenta dashed line), TiO$_2$ ARC (blue solid line), Si$_3$N$_4$ ARC (green solid line), and ZnS & MgF$_2$ dual layer ARC (magenta solid line).

Table 2.6: Solar-weighted reflectivity ($R_{AM1.5G}$) for all optimized ARCs.

	$R_{AM1.5G}$ for optimized ARCs				
Substrate Material	Bare Substrate	MgF$_2$	TiO$_2$	Si$_3$N$_4$	ZnS & MgF$_2$
InP	36.66 %	17.30 %	14.77 %	7.47 %	3.04 %
GaAs	40.79 %	20.86 %	14.96 %	8.58 %	4.50 %

entire visible spectrum.

Again using Equation 2.1 we can convert these reflectances to gain a quantitative understanding of the results in Figure 2.10. The results of these calculations are shown in Table 2.6, which presents the solar-weighted reflectances for the various coatings investigated in this thesis. These values validate the qualitative results from Figure 2.10, and show that Si$_3$N$_4$ is the highest performing single layer ARC, with a $R_{AM1.5G}$ about two times larger than that of the ZnS & MgF$_2$ dual layer

37
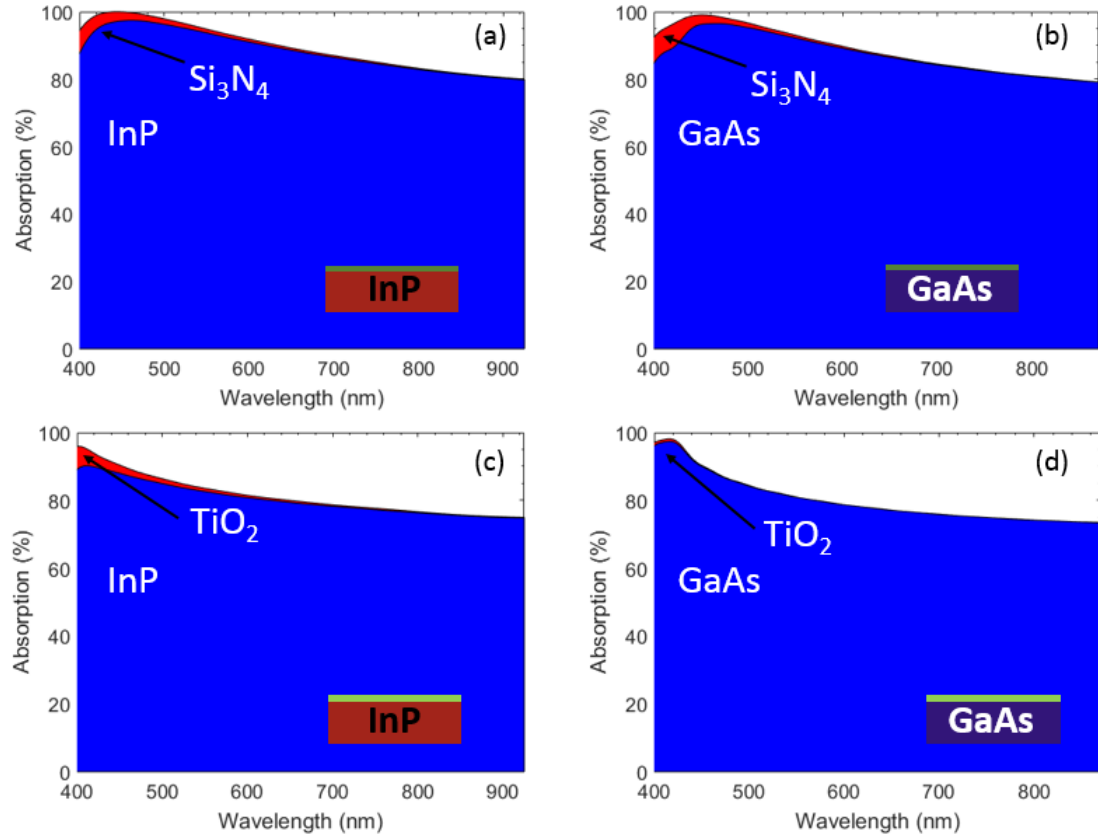
Figure 2.11: Spectrally resolved layer-by-layer absorption for select single layer ARCs on (a,c) InP and (b,d) GaAs. (a) and (b) show the results for the Si_3N_4 ARC while (c) and (d) show the results for the TiO_2 ARC. In all parts of this figure the blue region represents the absorption in the substrate while the red region represents the absorption in the coating layer.

ARC. Another important aspect of these results is that TiO_2 does not make a good single layer ARC on InP or GaAs, yet it makes the best material for our nanocylinder coatings. Possible explanations for this will be discussed in Chapter 3.

To make sure that these coatings were not absorbing much of the incident light we again ran the relevant simulations to determine the absorption in the ARC layers. In Figure 2.11 we see slight absorption in the coating layers at short wave-

lengths. However, unlike the ITO NCs, we do not see much absorption throughout the rest of the relevant spectrum. This is because, unlike ITO, these materials have fairly low extinction coefficients in the visible range, meaning that they are relatively ineffective when it comes to absorbing visible light. Again, using methods we have discussed in previous sections, we can determine how much solar-weighted absorption is present in both the ARC layer(s) and the substrate. We can see quantitatively from Table 2.7 and Table 2.8 that the amount of solar-weighted absorption in the single layer coatings is incredibly low, on average around 3 %. These values also validate that Si_3N_4 is the best material to use for a single layer ARC on InP and GaAs.

Table 2.7: Solar-weighted absorptivity ($A_{AM1.5G}$) in each layer for optimized ARCs on InP.

	$A_{AM1.5G}$		
Coating Material	Total $A_{AM1.5G}$	In InP	In coating
80 nm MgF_2	82.70 %	79.68 %	3.03 %
50 nm Si_3N_4	92.53 %	89.36 %	3.18 %
30 nm TiO_2	85.23 %	81.37 %	3.80 %

2.7 Angular Dependence of Reflection for Various Coatings

While all of the previous results covered in this chapter are important to help quantify the performance of the nanocylinder coatings and typical single and dual layer ARCs, it is critical to realize that all of these results are for normally incident light. Normally incident light is light from the sun which hits the photovoltaic de-

Table 2.8: Solar-weighted absorptivity ($A_{AM1.5G}$) in each layer for optimized ARCs on GaAs.

Coating Material	$A_{AM1.5G}$		
	Total $A_{AM1.5G}$	In GaAs	In coating
80 nm MgF$_2$	79.14 %	76.02 %	3.12 %
50 nm Si$_3$N$_4$	91.42 %	87.84 %	3.59 %
30 nm TiO$_2$	85.04 %	83.53 %	1.44 %

vice from an incident angle of 0°, or perpendicular to the device surface. However, this is not necessarily a situation that will occur in practice all of the time. While most concentrating photovoltaic systems employ complex solar tracking software and motors/actuators to move the panel to always have normally incident light, typical rooftop and extraterrestrial photovoltaic systems do not, meaning light can be incident on the device from various angles. As a result, antireflection coatings on these cells might not reflect light at different angles as well as from normal incidence, making angle-insensitive performance a key design aspect to make a better ARC.

In order to determine the performance of our ARCs for various angles of incident light, we needed to slightly modify our optical simulations. We do this by first, as expected, changing the incident angle of the plane wave source, which we can accomplish by a direct change of a setting on the source in the simulation. Because this is an adjustable parameter, we can set up a parameter sweep where we cycle through a wide variety of incident angles for our plane wave source. For our simulations we chose angles from 0° - 70° in intervals of 10°. However, the slight change of incident angle means our in-plane periodic boundary conditions are in-
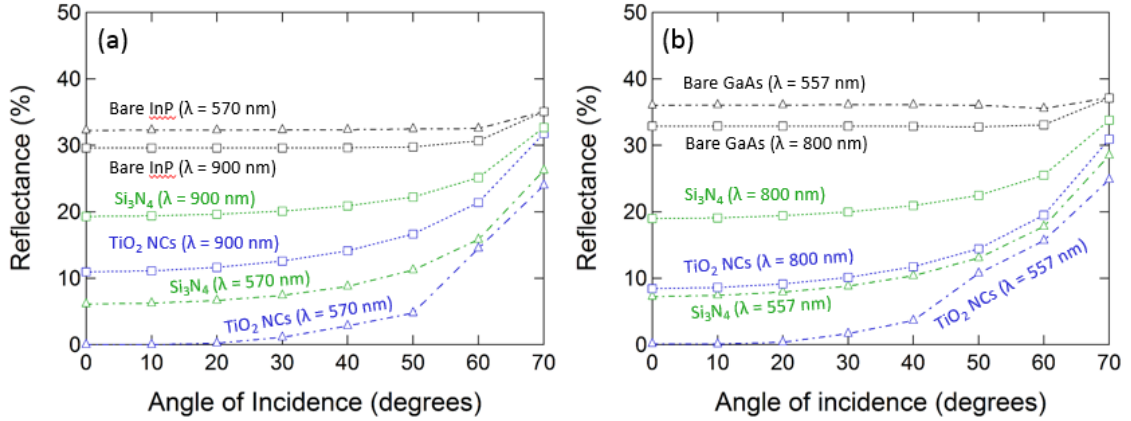
Figure 2.12: Angularly resolved reflectance for various coating structures on (a) InP and (b) GaAs. Both plots show the reflectance as a function of incident angle for the bare substrate (black), the 50 nm thick Si_3N_4 ARC (green) and the optimized TiO_2 NC coating (blue) averaged over both polarizations. For (a) InP the data is shown for wavelengths of $\lambda = 570$ nm (triangles, dashed lines) and $\lambda = 900$ nm (squares, dotted lines). For (b) GaAs the data is shown for wavelengths of 557 nm and 800 nm. The two wavelengths chosen for each active material were characteristic of a reflectance minima and a value close to the bandgap wavelength for each material.

correct, because the propagating light from one unit cell of the simulation to the next will not be exactly periodic. Portions of the incident plane wave will be out of phase with other portions by some non-zero amount. To correct for this phase factor, Lumerical provides the option of using Bloch boundary conditions, where we can include this phase difference in the calculation of the fields via a simple Bloch formalism, namely an exponential phase factor multiplying the field magnitudes.

We can see the results of these simulations in Figure 2.12 for the best single layer ARC and nanocylinder coating. When we performed the simulations we ran one set with p-polarized light and another set with s-polarized light, then averaged

the results to arrive at the data presented in Figure 2.12 for light with an average polarization. It is not entirely unexpected that for a wavelength where a reflectance minimum occurs for these structures that the angularly resolved reflectance will also be minimal. What is interesting, however, is that for both the Si_3N_4 ARC and the TiO_2 NCs on both substrates the reflectance is on average fairly angularly insensitive before 45°. This is a good indication, especially for our TiO_2 nanocylinder coating, that our designs can hold up with the industry standards for ARCs, even surpassing them in angle-insensitive performance for most relevant incident angles.

2.8   Overall Results and Discussion

In this chapter, we have described and presented the results of our optical simulations for various antireflection coating designs. We have also covered the main optical design structures of this thesis, namely the nanocylinder array coatings, single layer ARCs, and even a dual layer ARC. Here we will discuss some of the overall results of our simulations with these coatings and some potential conclusions that can be drawn from them.

2.8.1   Coatings

In terms of comparing the various coating structures, we will use solar-weighted average reflectivity as our metric of comparison, taking into account both reflectance from the structure as a whole and the light absorbed in the coatings themselves. We first examine the characteristics of all of the nanocylinder coatings used in this
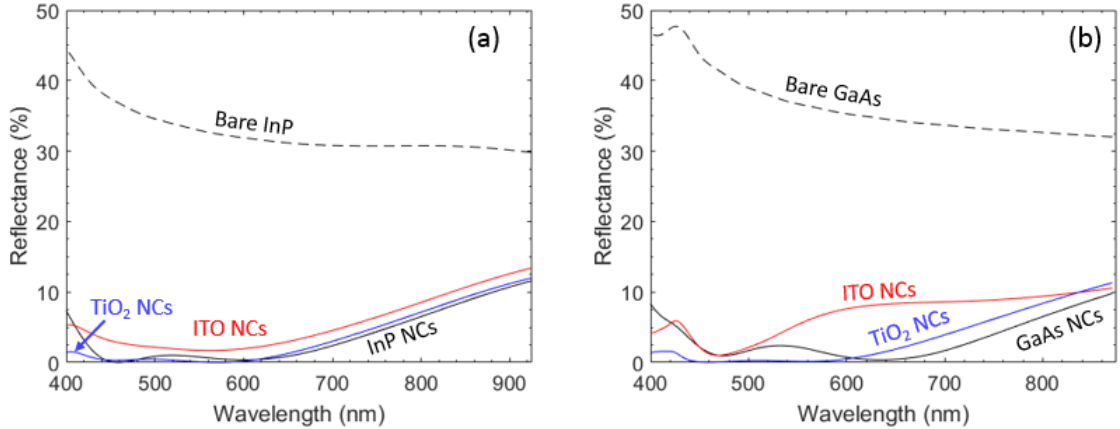
Figure 2.13: Spectrally resolved reflectance of all NC coatings on (a) InP and (b) GaAs. Both plots show the reflectance for the following coatings: bare substrate (black dashed line), active material NCs (black solid line), ITO NCs (red solid line), and the TiO_2 NCs (blue solid line).

Table 2.9: Solar-weighted reflectivity ($R_{AM1.5G}$) for all optimized nanocylinder coatings.

	$R_{AM1.5G}$ for optimized NCs			
Substrate Material	Bare Substrate	Substrate NCs	ITO NCs	TiO_2 NCs
InP	36.66 %	3.68 %	3.34 %	1.25 %
GaAs	40.79 %	4.72 %	4.45 %	1.23 %

study. The spectrally resolved reflectances for all of our optimized nanocylinder coatings are shown in Figure 2.13, while the solar-weighted reflectances are shown quantitatively in Table 2.9. For a bare substrate with no optical coating, the solar-weighted reflectance is 37 % for InP and 40.8 % for GaAs, much larger than any option with a nanostructured coating. Recalling from Table 2.6 that our best ARC, Si_3N_4, resulted in a solar-weighted reflectance of 7.5 % for InP and 8.5 % for GaAs, we note that all of our nanostructured coatings optically outperform even the best

single layer ARC. Additionally, our nanocylinder array coatings carry the additional benefits of significant broadband reflectivity suppression throughout the visible spectrum and angle insensitivity for many incident angles. Even with the substantial absorption in the ITO layer for our ITO NCs, the other nanostructured coatings facilitate greater solar-weighted absorption in the active photovoltaic material than a single layer coating (Table 2.3, Table 2.5, Table 2.7, Table 2.8).

In terms of the nanostructured coatings themselves, it is clear that TiO_2 is the best material to use for these types of structures on these III-V photovoltaic materials. While the index of TiO_2 might not match exactly with the optimal index for a single layer ARC, the nanocylinder architecture provides the benefits of broadband reflectance suppression, small absorption in the coating layer, and angle-independent reflectivity at short-to-intermediate incident angles (Figure 2.4, Figure 2.5, Figure 2.12). While it is beneficial to learn that ITO makes a viable nanostructured coating on these materials, the large amount of absorption in the ITO layer makes it much less practical in terms of its implementation in a real device. However, using it as a sacrifical layer for charge mediation purposes in FIB fabrication of these nanostructured coatings may be a possible option for the material, especially because we can see from our results that it does not significantly compromise the optical performance. The active material nanostructures perform well compared to a single layer ARC, but are the worst nanostructures in terms of optical performance, with the added drawback of requiring nanostructuring of the active material.

We can also compare the performance of the nanostructured coatings with
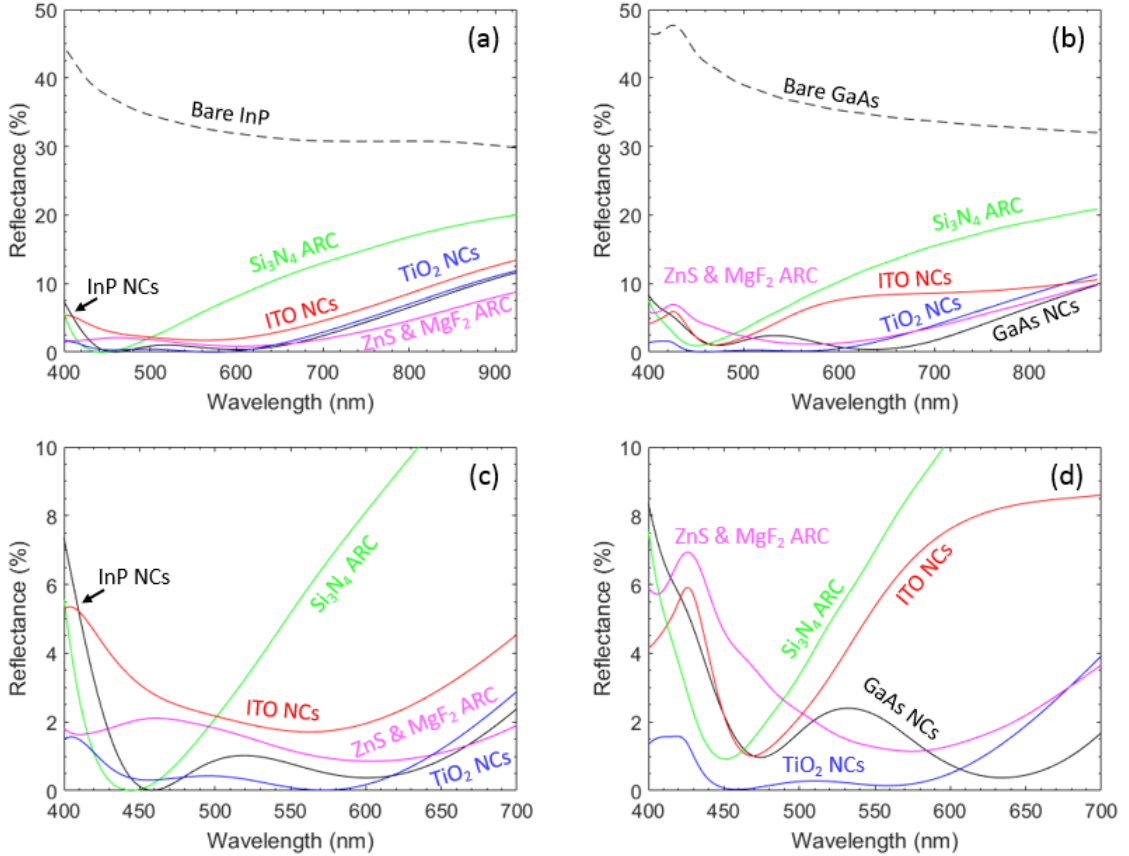
Figure 2.14: Spectrally resolved reflectance of various coatings on (a) InP and (b) GaAs. (c) and (d) show zooms of the visible spectrum region for all coatings on InP and GaAs, respectively. All NC coatings have the same colors as in Figure 2.13, while the Si_3N_4 ARC (green line), and the dual layer ZnS & MgF_2 ARC (magenta line) are also represented in these plots.

the single and dual layer ARCs (Figure 2.14). Here, both the substrate and TiO_2 NCs have lower reflectances over the visible range than even the dual layer ARC. This is another validation that our nanostructured coatings can outperform even the best dual layer coatings. We can gain further insight by comparing their solar-weighted reflectances. With a solar-weighted reflectance of $\sim 1.3\%$ over the spectral range (Table 2.2), the TiO_2 NCs again surpass the performance of the optimized

dual layer ARC (3.1 % solar-weighted reflectance) used in the world record InP solar cell [22]. The optical advantages of these nanostructured coatings provide compelling reasons to use them for light absorption enhancement compared to typical ARCs. It is important to note, however, for these direct bandgap materials (InP and GaAs), the antireflection properties of the nanostructures become more important than the light trapping properties. This is because nearly 95% of the entering light (at λ = 900 nm in InP) can be absorbed within a 1 μm InP cell with a back reflector. However, for a 1 μm Si cell with a back reflector to absorb a similar fraction of the above bandgap spectrum, a light trapping factor (*i.e.* path length enhancement) of 16 would be needed. Thus, for thin-film ($\sim$ 1 μm) direct bandgap semiconductors, the design of high quality antireflection coatings is of greater importance.

2.8.2 Photovoltaic Materials

As we see from the results of these optical simulations, there are almost no differences between using InP and GaAs as the active photovoltaic material, in terms of designing nanostructured coatings and grading their optical performance. The reflectance spectra from nanostructures on both materials are extremely similar and only differ quantitatively by a few percent. While the GaAs structures result in larger solar-weighted reflectances, part of this can be attributed to the larger bandgap of GaAs, preventing light from 871 nm - 925 nm from being absorbed. However, the power density in the solar spectrum at these wavelengths is low, so another possible explanation might be the slightly higher index of refraction in

GaAs compared to InP. Despite these small differences, the performance of these nanostructured optical coatings are similar across both material systems, indicating that the optical enhancement gained from using the nanostructures is a result of design or geometry rather than compatibility with a particular photovoltaic material. Overall, the results from this chapter provide strong evidence that optically designed nanostructures have significant potential as antireflection layers, and that this effect is not limited to Si but may be beneficial for many thin-film high index absorber materials, such as InP and GaAs.

Chapter 3:   Investigation of Optical Mechanisms

In this chapter, we will dive into the underlying mechanisms responsible for the optical enhancement provided by the nanocylinder array coatings on III-V solar cells. We will present studies of the electrical field intensities around the nanocylinders and compare them to previous results to support the idea of a Mie-like resonance effect provided by the nanostructures. Additionally, we will describe investigations into the specific optical modes of the nanocylinder arrays, revealing that a combination of the Mie-like resonance effect and an effective index model accurately describes the overall enhancement of the nanostructured coatings.

3.1   Electric Field Intensity Profiles

When thinking about what would reveal the underlying physical mechanisms responsible for the antireflection effects of our nanocylinder arrays, the first place we turned to was previous work with these nanostructures on Si. The work by Spinelli et. al. (Ref. [12]), highlighted the importance of examining the distribution of the electric field around and inside the nanocylinder itself. By examining the electric field intensity distribution, we can visualize the field coupling between the nanostructure and the substrate, as well as examine variations in the geometrical modes of

light inside the nanocylinder [12]. We again turned to Lumerical FDTD simulations to accomplish this task. In these simulations, because we are only examining one isolated nanocylinder, we used a finer mesh around the nanoclyinder volume with only 1 nm mesh spacing. The fine mesh drastically increases computational time, but yields results with much higher resolution so that we can clearly visualize all of the features of the field intensity distribution in and around the nanocylinder. For ease of simulation and visualization, we created two 2D cross-sectional field intensity monitors in these simulation, both splitting through the center of the nanocylinder, one in the XZ plane and one in the YZ plane. This method allowed us to acquire a full set of results to visualize the internal field intensity profile in the nanocylinder.

For these simulations we utilized a total-field scattered-field (TFSF) method, using Lumerical's option for a TFSF plane wave source. A total-field scattered-field calculation is typically used to calculate the field from optically scattering structures. In Lumerical, the TFSF source separates the simulation volume into two regions - one where the total field is calculated (incident field + scattered field), and another where only the scattered field is calculated. The incident plane wave is injected normally to the surface, in our case in the $-\hat{z}$ direction, and at the boundaries of the source region the incident field is subtracted, leaving only the scattered field outside of the volume enclosed by the source. We completely enclosed the nanocylinder in the source volume, so that the field calculated inside the nanocylinder is the total field plus the scattered field. The field calculated outside the nanocylinder volume is exclusively the scattered field. This simulation allows us to directly visualize the field coupling from the nanocylinder into the substrate, by seeing only the scattered

49

field outside of the nanocylinder volume.

We ran our field intensity profile simulations for a few specific wavelengths, namely wavelengths where there were minima in the reflectance spectra for the various optimized structures we investigated. For example, for the optimized InP NCs there were two minima in the reflectance spectrum, one at $\lambda = 458$ nm and another at $\lambda = 599$ nm, while for the optimized GaAs NCs these minima occurred at $\lambda = 474$ nm and $\lambda = 634$ nm. The results of these field intensity profile simulations are shown in Figure 3.1. We can clearly see the field intensity distributions in and around the nanostructures, as well as the similarities between them for the individual reflectance minima. For each wavelength the field intensity profiles are extremely similar across both substrate materials. In all of the structures we see a few similar characteristics: two high field intensity lobes at the top corners of the nanocylinder, a large scattered field in the substrate, and a dome-like intensity region inside the nanocylinder. All three of these features are consistent with previous results for these nanostructures on silicon [12], indicating that the optical enhancements provided by the nanostructures are not necessarily material dependent. Specifically, the large forward scattering of the field from the nanoclyinder into the substrate is an indication of a leaky optical mode in the high index substrate for light that is resonantly confined in the nanocylinder [12]. This facilitates increased in-coupling of light into the substrate and provides a mechanism which may explain the beneficial antireflection effects of the nanocylinders.

We find similar results when we examine the field intensity profiles for the TiO$_2$ NCs on InP and GaAs. Looking at the profiles in the context of the spectrally
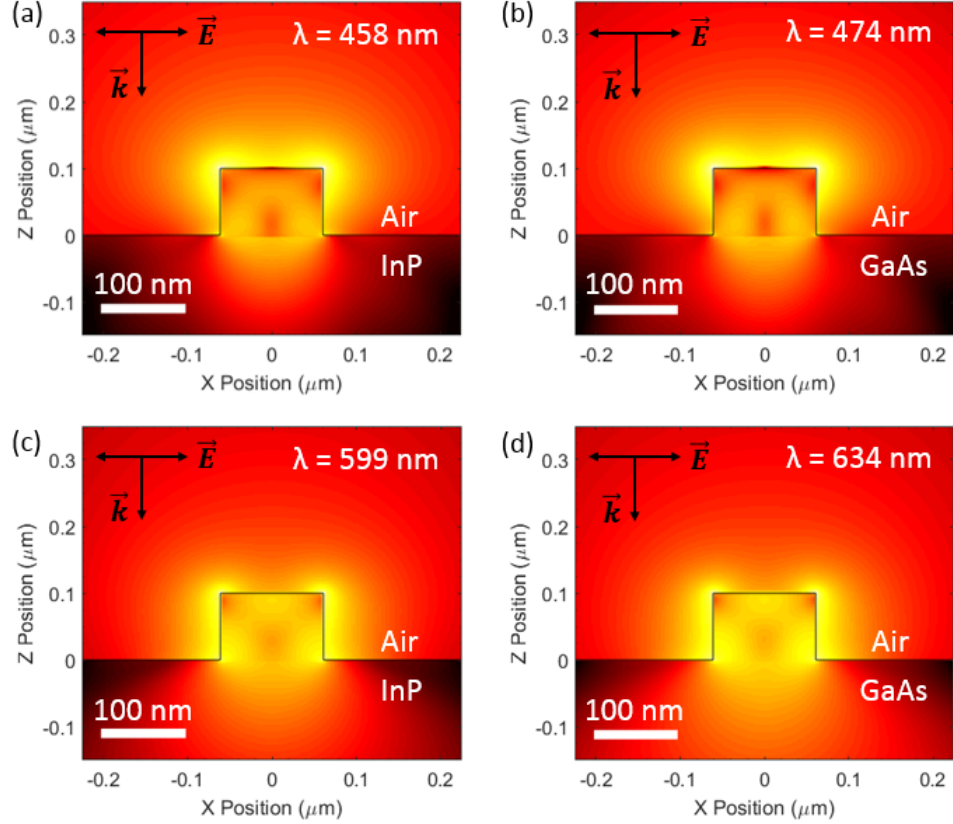
Figure 3.1: Electric field intensity profiles for optimized (a,c) InP and (b,d) GaAs NCs at wavelengths where there were minima in the reflectance spectrum. All colorscales are the same and the plots show the logarithm of the field intensity spatially distributed in the XZ cross section of the nanocylinder. The schematic in the top left of each image shows the electric field polarization direction and the wavevector of the incident plane wave. The scale bar in the bottom left indicates 100 nm in the simulation.

resolved reflectance (Figure 3.2), we can see that they maintain many of the same

characteristics as those for the active material nanostructures - two high intensity

lobes at the corners of the nanocylinder and large forward scattering of the field in

the substrate. However, the high intensity lobes seem to stretch across the entire

side of the nanocylinder, in addition to a high intensity region in the TiO_2 spacer
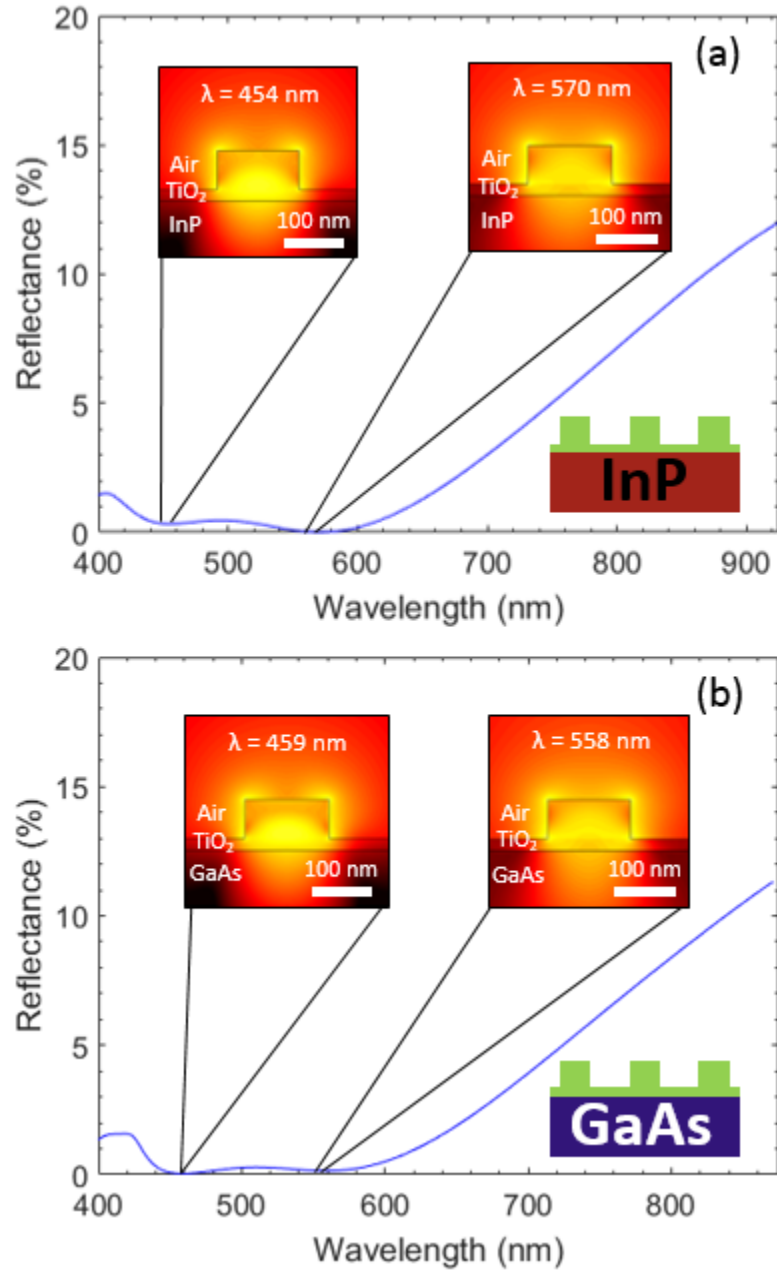
Figure 3.2: Spectrally resolved reflectance and electric field intensity profiles for optimized TiO$_2$ NCs on (a) InP and (b) GaAs. All colorscales, field polarizations, and cross sections are the same as Figure 3.1.

layer between the nanocylinder and the substrate. This is likely an indication of

the differences in material between the spacer layer, nanocylinder, and substrate,

because we would expect different optical enhancement with a nanocylinder of a different index of refraction as the substrate. Another possible explanation for the enhancement in the spacer layer will be provided later in this chapter. Finally, we see little difference between the field intensity profiles for the NCs on InP versus those on GaAs.

Looking at the field intensity profiles for the optimized ITO NCs (Figure 3.3), we see similar results to the TiO$_2$ NCs with high intensity lobes on the sides of the nanocylinders and large forward scattering of the fields into the substrate. However, in the ITO structures we see much larger field intensities throughout the nanocylinder volume, especially for the ITO NC on the GaAs substrate in Figure 3.3(b). Overall, the field intensity profiles for all of our nanostructured coatings show that large forward scattering into leaky optical modes in the substrate is likely a primary optical mechanism which describes the enhancement of the NCs over traditional
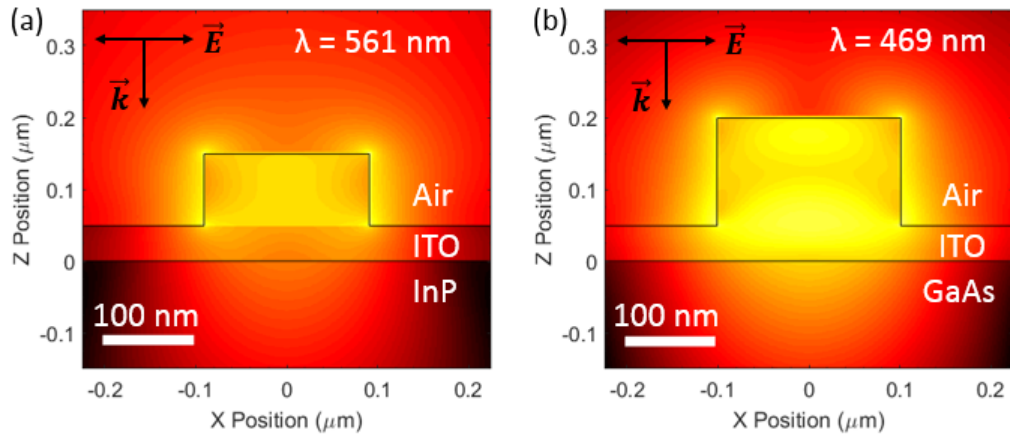
Figure 3.3: Electric field intensity profiles for optimized ITO NCs on (a) InP and (b) GaAs. All colorscales, field polarizations, and cross sections are the same as Figure 3.1.

ARCs.

3.2   Probing Optical Modes

We can gain further insight into the optical mechanisms behind the advantages of these nanostructured coatings by considering the spectrally resolved reflectance of the structures as a function of NC diameter and period. Variations in the reflectance versus nanocylinder diameter can reveal information about localized modes in these structures, while pitch (*i.e.* period) variations can uncover information about the coupling between different nanostructures as a result of grating and diffraction effects. These investigative methods allow us to identify specific optical modes in the nanostructured coatings. Because we already have all of the relevant data from previous optimizations and geometry sweeps from earlier simulations, no new simulations were needed to acquire this data. For these results, we chose to focus on the TiO_2 and ITO NCs, because those are the two primary nanostructured coatings we wanted to investigate.

We can see the results for the TiO_2 NCs on InP (Figure 3.4) and GaAs (Figure 3.5) in the following figures. In both figures, there are two large regions of minimal reflectance coinciding with minima in the reflectance spectrum for the optimized geometry. This can be explained by the combination of two different optical effects, as described in the following sub-sections.
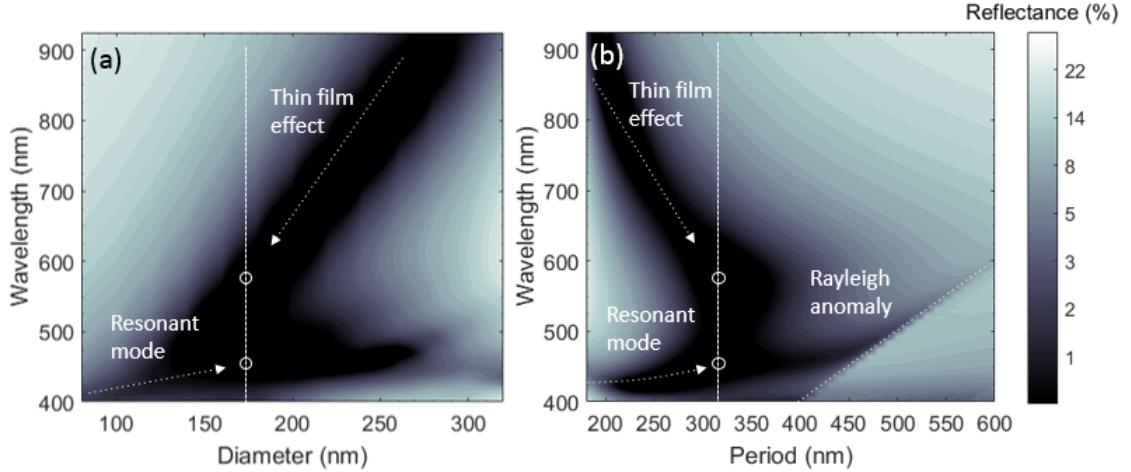
Figure 3.4: Spectrally resolved reflectance as a function of (a) NC diameter and (b) period for TiO$_2$ NCs on InP. In part (a) the period is fixed at 320 nm and in part (b) the diameter is fixed at 180 nm. For (a) and (b) the dashed lines indicate the dimensions of the optimized structure, the circles indicate positions of local minima in the reflectance spectrum, and the dotted lines indicate spectral features that can be described by specific optical effects.

3.2.1 Mie-like Resonant Mode

The first of these optical effects is that of a Mie-like resonance, which originates at wavelengths between 400 and 450 nm for small nanocylinder diameters and intersects with the optimized geometry at the first local minimum in the reflectance spectrum ($\lambda = 454$ nm for InP (Figure 3.4), $\lambda = 459$ nm for GaAs (Figure 3.5)). We call this a Mie-like resonance because proper Mie resonances occur for spheres of material in air, in accordance with how Gustav Mie originally discovered his solutions to Maxwell's Equations for the scattering profiles of such objects. In practice, Mie scattering refers to the scattering from structures with sizes on the order of the wavelength of the incident light/field, which applies to our nanostructured antire-
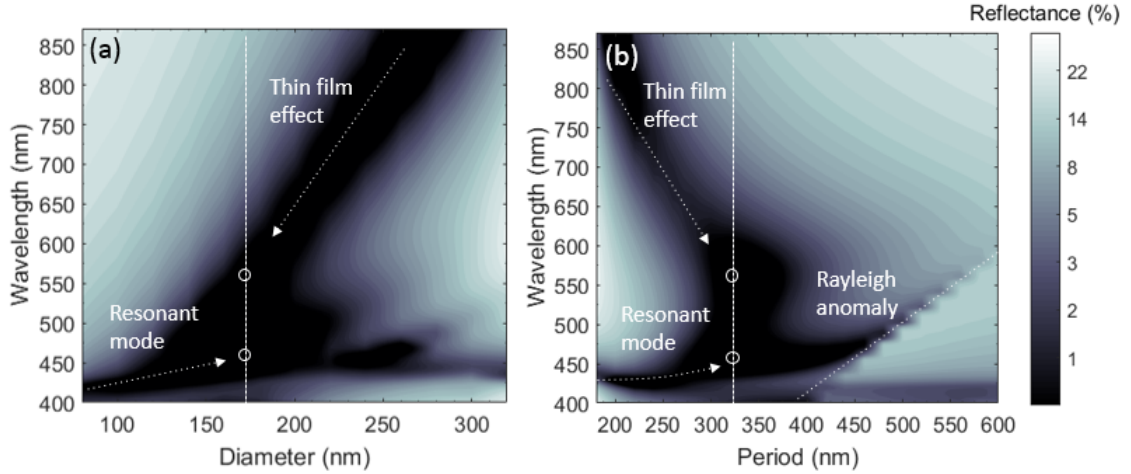
Figure 3.5: Spectrally resolved reflectance as a function of NC diameter (a) and period (b) for TiO$_2$ NCs on GaAs. All aspects of these plots, including the dimensions of the optimized NCs, are the same as those in Figure 3.4.

flection coatings. We have, in essence, already validated the existence of this mode via the field intensity profiles from Figure 3.2. The field profiles contain two high intensity lobes at the top corners of the nanocylinder and strong forward scattering into the substrate. As stated previously and verified in previous work, this is primarily the result of light from a Mie-like resonance in the nanostructure coupling into leaky optical modes in the high index InP or GaAs substrate [12].

This short-wavelength resonant mode is present in these modal investigations of both of our nanostructured coatings. While it is less evident in the NC diameter and period variations for our ITO NCs (Figure 3.6 for InP, Figure 3.7 for GaAs), the presence of the mode is still validated by the field profiles in Figure 3.3. In the modal investigations, especially for the ITO NCs on GaAs in Figure 3.7, the resonant mode results in a strong reflectance minimum across most if not all
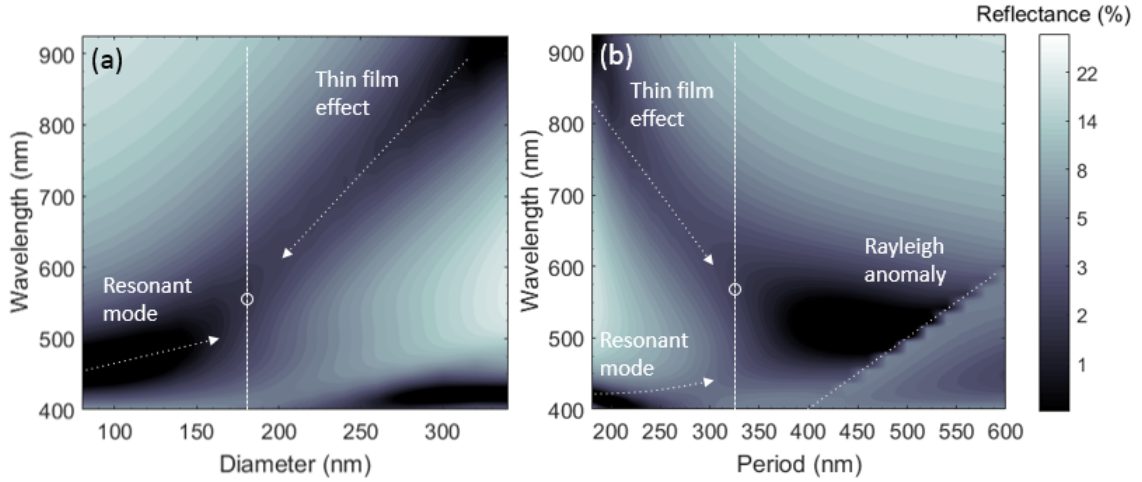
Figure 3.6: Spectrally resolved reflectance as a function of (a) NC diameter and (b) period for ITO NCs on InP. In (a) the period is fixed at 340 nm and in (b) the diameter is fixed at 180 nm. The dashed lines, circles, and dotted lines have the same significance as in Figure 3.4.
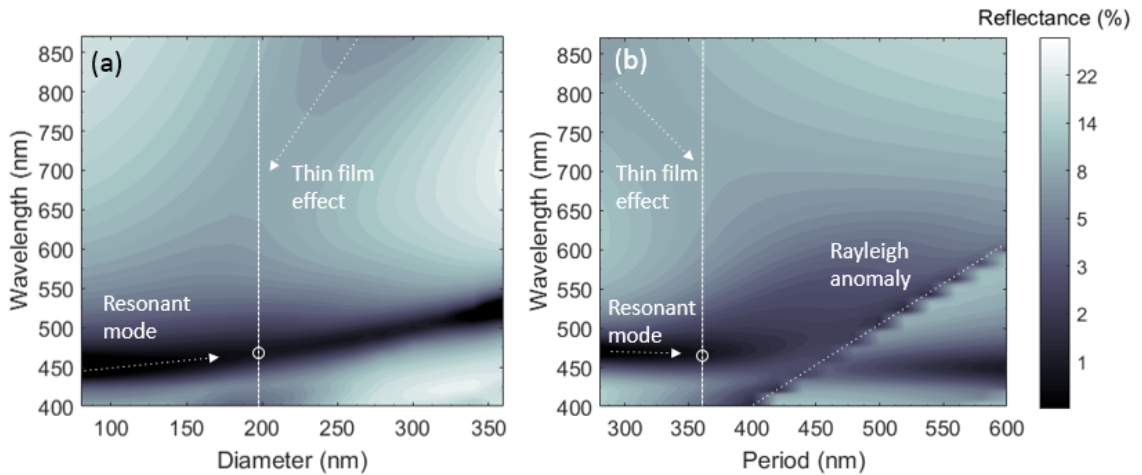
Figure 3.7: Spectrally resolved reflectance as a function of (a) NC diameter and (b) period for ITO NCs on GaAs. In (a) the period is fixed at 360 nm and in (b) the diameter is fixed at 200 nm. The dashed lines, circles, and dotted lines have the same significance as in Figure 3.4.

geometries. The resonant mode also lines up well with the reflectance minimum for the optimal geometry for the GaAs case, providing strong evidence that it is the primary optical mechanism responsible for the minimized reflection of that structure. It is important to keep in mind that, while the resonant mode is present in both of these modal plots, the more important case for the Mie-like resonance is the diameter variations case, because that will reveal more information about localized modes within the individual nanocylinders.

3.3   Thin-Film Effect - Effective Index Model

The second of the optical effects evident in these modal studies is present for the TiO$_2$ NCs in the second minimal reflectance region, seen near $\lambda = 570$ nm for InP (Figure 3.4) and near $\lambda = 558$ nm for GaAs (Figure 3.5). This minimal reflectance region is more pronounced for diameters larger than the optimum and for array periods smaller than the optimum (labeled as thin-film effect in Figure 3.4), and can be attributed to a thin-film effect provided by the nanocylinders acting as a layer with an effective refractive index. The mixture of the high index TiO$_2$ (or ITO) nanocylinders and the surrounding air acts as a thin-film with a thickness governed by the nanocylinder height and an effective index that is calculated as a volume weighted average of the refractive indices of the two materials (TiO$_2$ (or ITO) and air):

$$n_{eff} = n_{TiO_2}(\frac{\pi d^2}{4p^2}) + n_{air}(1 - \frac{\pi d^2}{4p^2}), \tag{3.1}$$

where n_{TiO_2} is the refractive index of TiO$_2$, $n_{air} = 1$, d is the nanocylinder diameter, and p is the periodicity.

3.3.1 Dual Layer ARC Configuration

In fact, the entire structure can be approximated as a dual layer ARC, with a top layer described by the effective index determined by the nanocylinders (Equation 3.1) and a bottom layer described by the TiO$_2$ spacer layer (Figure 3.8). To verify this effect, we ran optical simulations of a dual layer ARC with a top layer consisting of an effective index determined by Equation 3.1 (representing the NCs)
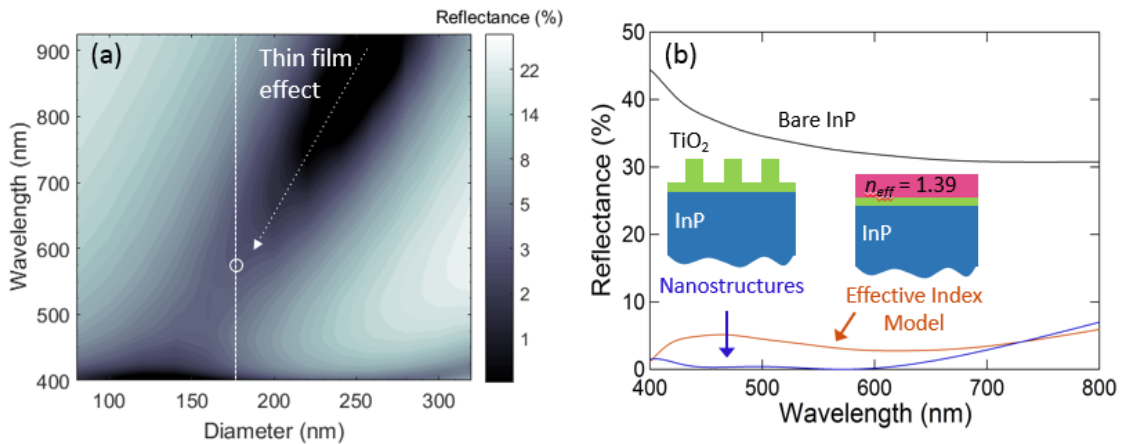
Figure 3.8: Optical performance of a dual layer ARC on InP with a top layer of an effective refractive index replacing the TiO$_2$ NCs. (a) Reflectance of an effective dual layer ARC on InP as a function of wavelength and NC diameter for a period of 320 nm and height of 100 nm. The top layer has a thickness equivalent to the NC height and an effective index calculated using Equation 3.1. The bottom layer is the 30 nm thick TiO$_2$ spacer layer. The dashed line, circles, and dotted lines have the same significance as Figure 3.4. (b) Comparison between the reflectance spectra for the optimized nanostructured device and a simple effective index model for this optimized NC geometry.

and a bottom layer of 30 nm of TiO_2 for the spacer layer. The results are shown in Figure 3.8(a), which indicate clear quantitative and qualitative agreement with the data from Figure 3.4, capturing the thin-film effect for long wavelengths and large NC diameters. For the optimized geometry (Figure 3.8(b)), the dual layer ARC model accurately reproduced the long-wavelength broadband reflectance suppression while missing the short wavelength reflectance minimum due to the resonant mode. We can see these results replicated for the ITO structures on InP and GaAs in the figures below (Figure 3.9 and Figure 3.10).

3.3.2 Rayleigh Anomaly

Additionally, in Figure 3.4 there is another unique spectral feature characterized by reflectance minima at wavelengths equivalent to the array period. This feature is the consequence of a Rayleigh anomaly, which appears for similar structures on Si [12], and describes a dramatic change in the diffracted field from a grating as the result of a scattered wave emerging tangentially to the grating surface [34]. The scattered light traveling with a momentum in the plane of the nanocylinders is more strongly absorbed in the nanocylinders, causing the large reflectance dips in the spectrum at those specific wavelengths.
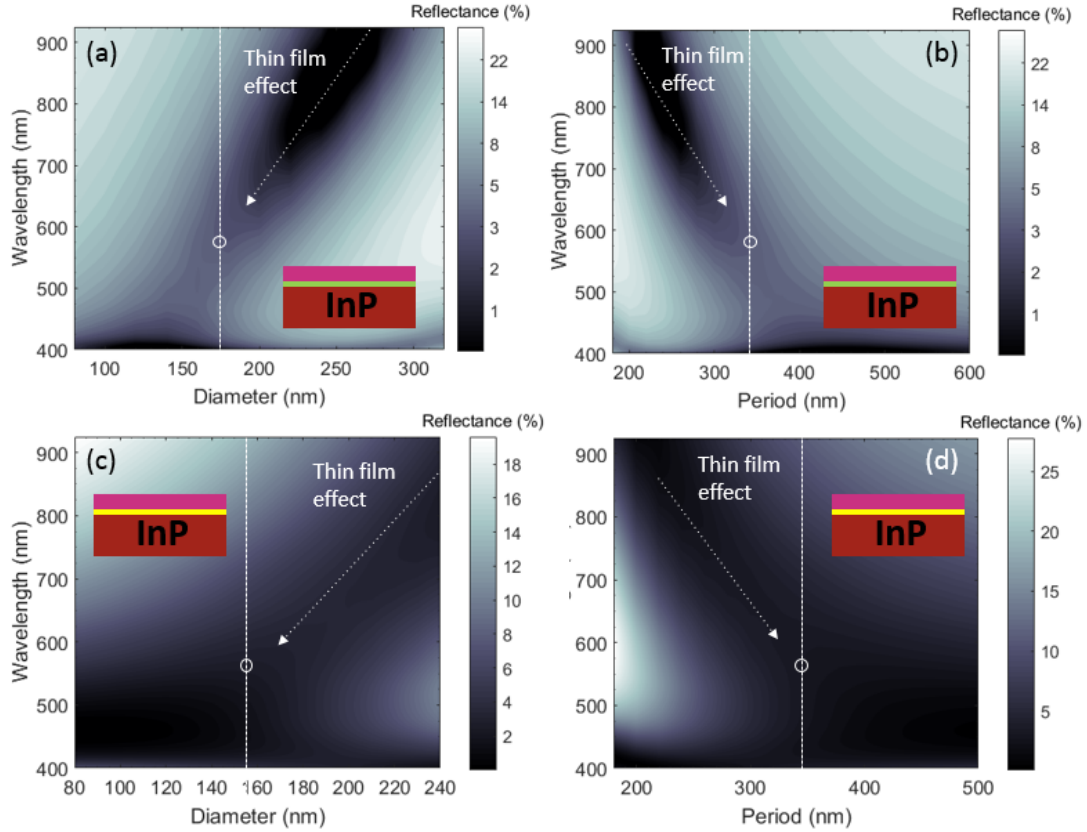
Figure 3.9: Optical performance of TiO$_2$ and ITO NCs on InP acting as a dual layer ARC with an effective index. (a) Same plot as Figure 3.8(a). (b) Same as (a) except varying the period and keeping a constant diameter of 180 nm. (c) and (d) are the same as (a) and (b) except using the optimized ITO NC geometries, where here, the bottom layer of the dual ARC is the 50 nm thick ITO spacer layer. The dashed line, circles, and dotted lines have the same significance as Figure 3.4.

3.4 Discussion

While the strategy to reduce reflection via a combination of Mie resonances and thin-film coating effects is quite general, the refractive indices of the materials used in this study are particularly beneficial. On its own, TiO$_2$ (with a refractive index of ~ 2.5 over the visible spectrum) is not a great thin-film dielectric antireflection

61
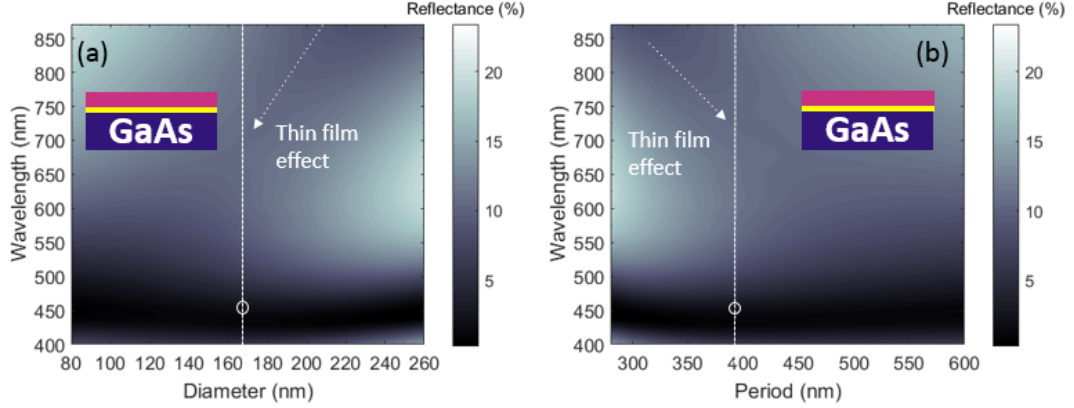
Figure 3.10: Optical performance of ITO NCs on GaAs acting as a dual layer ARC with an effective index. (a) Reflectance of a dual layer ARC on GaAs as a function of wavelength and NC diameter for a period of 360 nm and height of 100 nm. The top layer has a thickness equivalent to the NC height and an effective index calculated using Equation 3.1. The bottom layer is the 50 nm thick ITO spacer layer. The dashed line, circles, and dotted lines have the same significance as Figure 3.4. (b) Same as (b) except varying the NC period and keeping a constant diameter of 200 nm.

coating for InP due to its large index contrast with air, which we have seen from the results presented in Section 2.6. However, the inclusion of the TiO_2 NC coating layer (which has $n_{eff} = 1.39$ for the optimized structure), enables a graded index-like behavior. This combination of materials yields an index of refraction profile that more gradually transitions from air ($n_{air} = 1$) to InP ($n_{InP} = 3.7$) through the inclusion of two additional layers with $n_{eff} = 1.39$ and $n_{TiO_2} = 2.5$, thus yielding a better impedance match between air and InP. Similar results are expected for GaAs, and are clearly present with the ITO NCs. However, due to the parasitic absorption in the ITO layer, neither the effective index dual ARC effect nor Mie resonance accurately describe the effects of these structures.

Chapter 4:   Optoelectronic Device Performance

In this chapter we will examine the optoelectronic performance of our InP and GaAs photovoltaic devices with and without our nanostructured coatings. While the two previous chapters described our optical simulations, this chapter will focus on the combination of slightly modified optical simulations with electronic device simulations, utilizing another software package provided by Lumerical (Lumerical Device). We will describe how we can take the results from these optical simulations and use them as inputs into the electrical simulations to see how the solar cell performs electronically, extracting important solar cell device parameters to quantify how a realistic device using our structures would perform. Then, in a further effort to quantify the performance of a real device utilizing these structures, we perform optical simulations of our cells in a module-like architecture with a glass front interface and an encapsulant. All of these results help validate our design as being viable for a realistic and functional photovoltaic device.

4.1 Electrical and Device Simulations

4.1.1 Optical Simulations with a Device-like Architecture

In order to quantify the device performance enhancements resulting from our nanostructures, we use the results from optical simulations as inputs in electrical device simulations to determine the expected power conversion efficiencies. For these new optical simulations, we again use the FDTD method and keep almost all of the parameters the same except for a few key parts. First, we vary the InP and GaAs substrate thicknesses for three different thicknesses, 0.5 μm, 1 μm, and 2 μm (Figure 4.1, Figure 4.2). These thicknesses are typical for thin-film photovoltaic devices and provide a range of thicknesses for which we can investigate the optoelectronic performance of our devices. For these simulations the entire simulation region must enclose the volume of the substrate as well, because we are simulating a finite substrate thickness. We also decided to include an ideal metal back reflector as the boundary condition for our simulations at the back surface of the substrate. Back reflectors are a typical optical design method for photovoltaic cells, used to reflect light back into the cell that might otherwise transmit through it and to limit the cell's emission angle (i.e. no light can escape through the back). We will use the results from these optical simulations as inputs into our electronic simulations.

Because our simulation region now encompasses the entire substrate thickness rather than just the first few hundred nanometers, we can calculate the spatially resolved absorption throughout the entire InP or GaAs substrate. Using this spa-
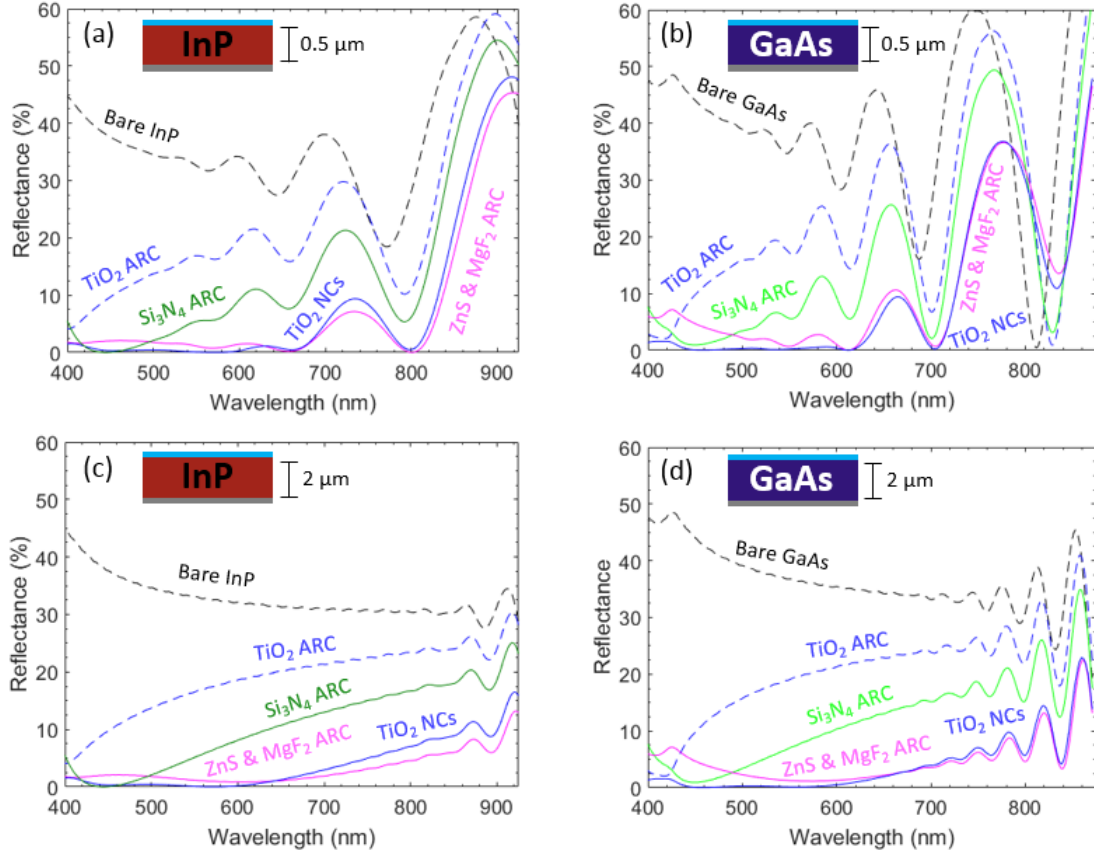
Figure 4.1: Spectrally resolved reflectance of various coating structures on (a,c) InP and (b,d) GaAs thin-film solar cells with active layer thicknesses of (a,b) 0.5 μm and (c,d) 2 μm. All cells simulated have the device-like architecture described in this section. The coatings investigated were: bare substrate (black dashed lines), TiO$_2$ ARC (blue dashed lines), Si$_3$N$_4$ ARC (green lines), ZnS & MgF$_2$ dual ARC (magenta lines), and the TiO$_2$ NCs (blue lines).

tially resolved absorption profile, we can calculate the electron-hole pair generation rate, assuming one electron-hole pair is generated per absorbed photon [9]. This rate is used to determine the carrier dynamics in electrical device simulations using a finite-element based software platform (Lumerical Device) to solve the semiconductor drift-diffusion equations.
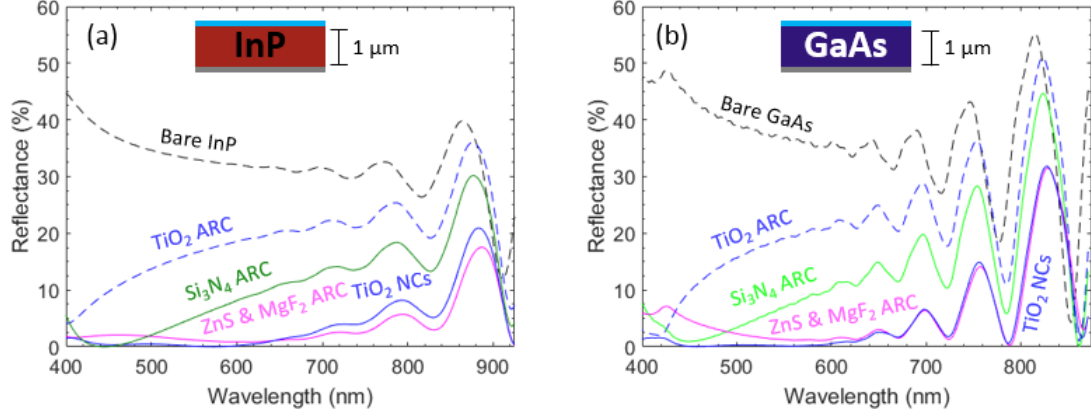
Figure 4.2: Spectrally resolved reflectance of various coating structures on 1 μm thick (a) InP and (b) GaAs thin-film solar cells. All cells simulated have the device-like architecture described in this section. The coatings and colors corresponding to the coatings are the same as those in Figure 4.1.

4.1.2 Motivation and Design Methodology

While we performed the optical simulations for both InP and GaAs, we decided to only perform the electrical simulations on the InP cells to provide a proof of concept. We design the photovoltaic device for the device simulations using a nominal p-i-n structure for a solar cell, with a background p-doping concentration of 10^{15} cm^{-3}. The cell is illuminated from the top surface, which consists of an 80 nm thick doped n$^+$ (10^{19} cm^{-3}) InP layer. Below lies the intrinsic p-layer with the background concentration, which makes up the base, and finally another 80 nm thick doped InP layer, this time with p$^+$ (10^{19} cm^{-3}) doping (Figure 4.3). This doping profile is optimized within reasonable limits and based on the generation rates within the active InP layer obtained from the optical simulations (Lumerical

FDTD). The optical data for these doped layers of InP is assumed to be the same as
that of the intrinsic material. We assume ideal ohmic contacts at flatband voltage
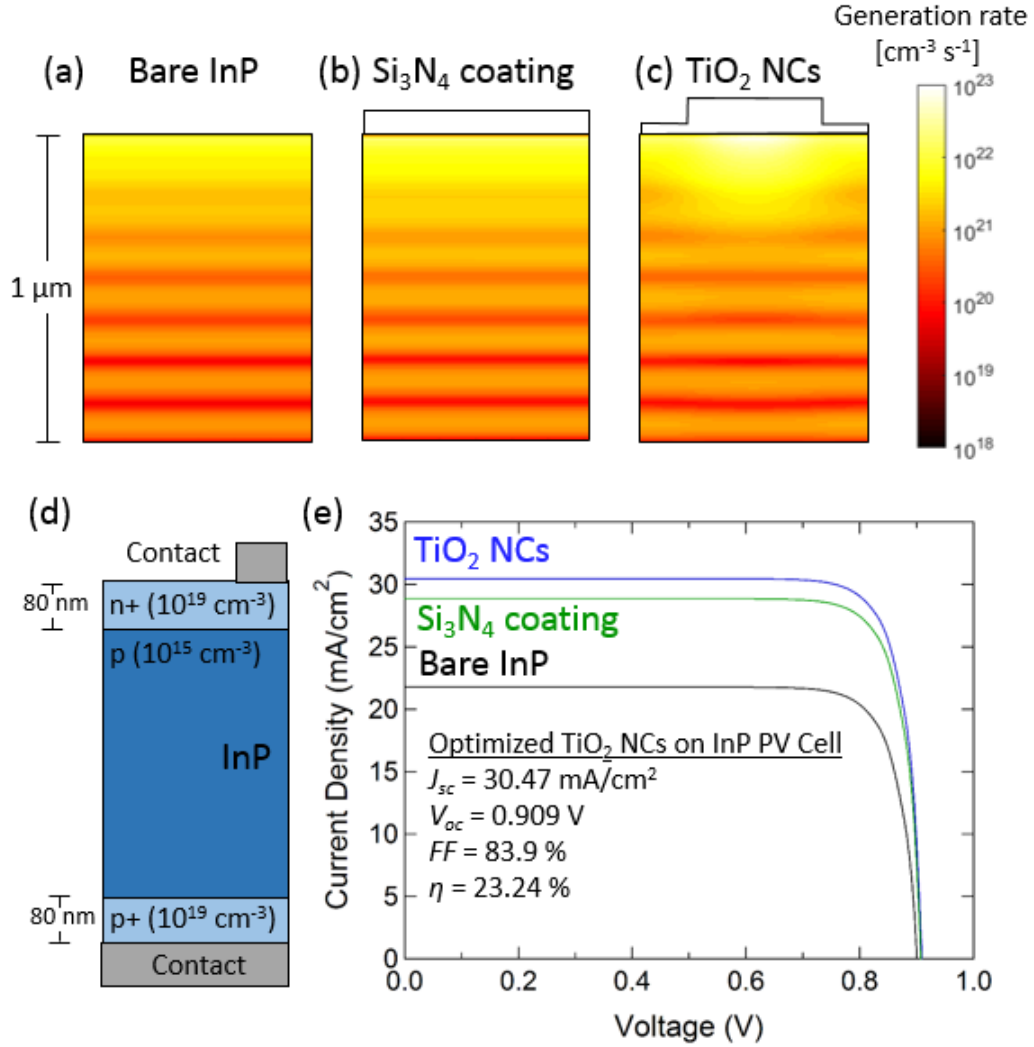
Figure 4.3: Generation rate profiles and J-V curves for InP solar cells with various coatings. Generation rate profiles were calculated via optical simulations of 1 μm - thick InP solar cells with an ideal metal back reflector and different optical coatings: (a) Bare InP, (b) 50 nm of Si_3N_4, and (c) optimized TiO_2 NCs. (d) Device parameters for p-i-n cell. (e) J-V characteristics for InP cells using the above coatings: bare InP (black), Si_3N_4 (green), optimized TiO_2 NCs (blue). Significant current density enhancement is found for our optimized TiO_2 nanophotonic coatings.

conditions, and the device model includes modest surface recombination velocities ($S = 10^7$ cm/s) at the interfaces between the active layer and the contacts [26]. The device simulations also incorporate radiative and non-radiative (Shockley-Read-Hall (SRH) and Auger) recombination mechanisms in the InP active layer. For SRH recombination, we use a bulk minority carrier lifetime of 10^{-8} s in the p-doped base layer and 3 x 10^{-6} s in the n-doped emitter. We assume a radiative recombination rate of 2 x 10^{-10} cm^3/s and an Auger coefficient of 9 x 10^{-31} cm^6/s. All of the above values were obtained from Ref [29]. and were utilized to recreate the electronic conditions seen in a real device.

4.1.3 Generation Rate Profiles and J-V Characteristics

As stated previously, optical simulations yield the generation rate profiles, integrated over the full spectrum to yield the number of electron-hole pairs generated per volume of InP per second (Figure 4.3). The three generation rate profiles shown were obtained for an InP layer thickness of 1 μm because they demonstrated the best optical and electrical performance. The generation enhancement is clearly seen in these images, as the carrier generation, particularly in the top half-micron of InP, increases for the Si$_3$N$_4$ and TiO$_2$ NC coatings compared to the bare InP. In particular, the strong forward scattering of light from the TiO$_2$ nanostructures into the InP results in a high generation rate in the top half of the cell. The various minima in the lower half of the generation rate profiles are due to optical interference effects

Table 4.1: Device results for InP solar cells with varied active layer thicknesses and optical coating structures.

InP Layer Thickness	0.5 μm			1 μm			2 μm		
Material	Bare InP	Si_3N_4	TiO_2 NCs	Bare InP	Si_3N_4	TiO_2 NCs	Bare InP	Si_3N_4	TiO_2 NCs
J_{sc} (mA/cm^2)	20.70	24.82	26.10	21.78	28.86	30.47	21.25	27.00	28.85
V_{oc} (V)	0.902	0.906	0.908	0.901	0.908	0.909	0.891	0.899	0.901
FF $(\%)$	85.9	86.1	86.1	83.3	83.8	83.9	80.1	80.2	80.82
η $(\%)$	16.04	19.36	20.41	16.35	21.96	23.24	15.16	19.47	20.85

between the incident light and the reflected light from the back reflector.

The calculated generation rate profiles are input into the electrical simulations, which calculate the specific solar cell device parameters as well as the J-V characteristics (Figure 4.3). Table 4.1 summarizes the results of our device simulations for each thickness of the InP active layer. The large short-circuit current density enhancement is clearly seen in the data, as expected due to antireflection effects provided by our nanostructured optical coating. The > 23 % efficiency of this device is a result of improved current density and voltage in our proposed design while simultaneously reducing cell thickness. However, the parameters of our simulation define idealized conditions, namely an ideal back reflector, idealized contacts, perfect periodicity, and no damage to the device due to additional processing. Some of these conditions may be unable to be met in a fabricated device, which would likely reduce the power conversion efficiency. We also note that the slight improvement of the fill factor as the active layer thickness is reduced (Table 4.1) is likely due to improved carrier transport and collection.

4.2 Module Configuration

4.2.1 Device Operation in an Encapsulant Environment

To further extend the practical implications of our design, we performed simulations to determine the effects of encapsulation of these cells in ethylene vinyl acetate (EVA), the industry standard for encapsulants in commercial solar modules. In order to accomplish this, we followed the methodology outlined recently by Spinelli et. al. [35]. We surrounded our InP and GaAs solar cells in EVA instead of air, including a variety of different coating structures in order to accurately compare the performance of our NC coatings to typical single and dual layer ARCs. We define a PML boundary condition at the top surface of the EVA to simulate a semi-infinite layer on the top surface. By including an additional 4.4 % reflection offset in our results from the glass-air interface of an actual module architecture [35], we can incorporate the effects of the glass cover and the encapsulant in one simulation. This design is because in typical solar modules the cells are surrounded by encapsulant and then encased in glass. In terms of the simulation structure for the solar cells themselves, we maintained the same simulation structure as with our optimizations from Chapter 2, with a semi-infinite substrate layer and normally incident illumination across the relevant spectral ranges for each photovoltaic material.

We can see results for a few of our coatings in Figure 4.4, where it is evident that the TiO_2 NCs still outperform both the ITO NC and Si_3N_4 coatings. Not only that, but we can see the vast difference between our devices when in EVA versus air by
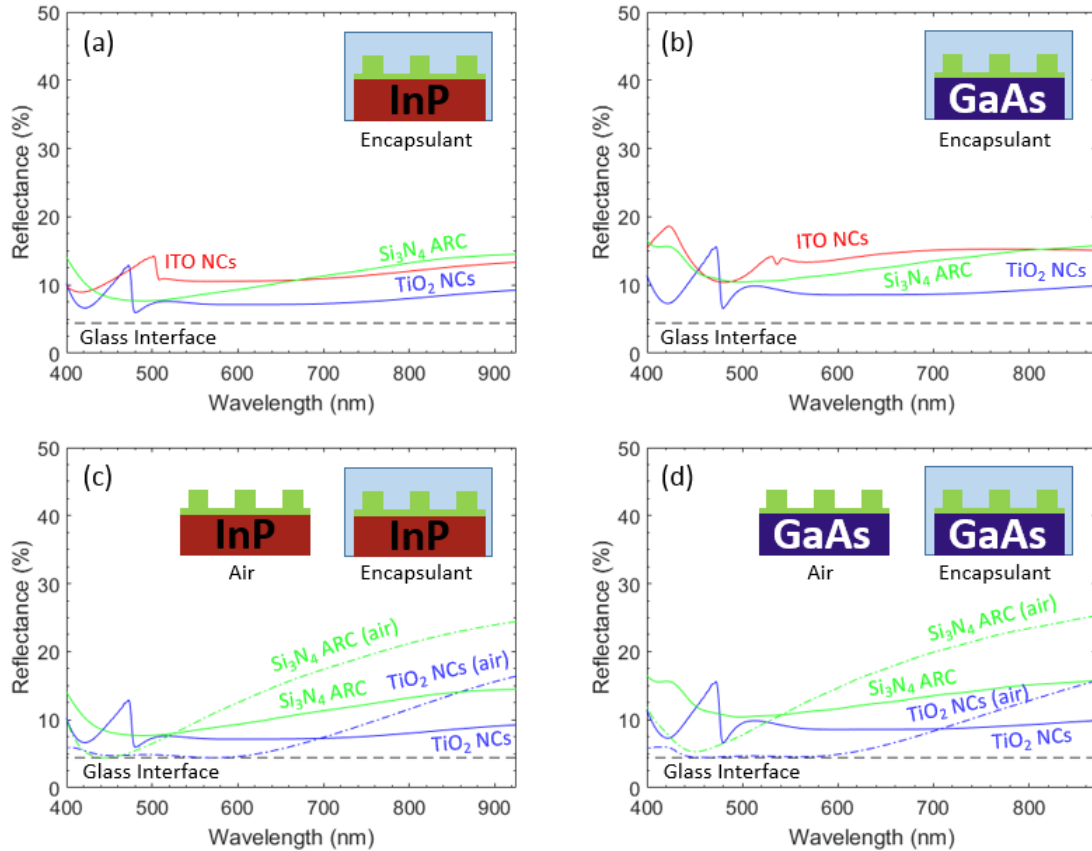
Figure 4.4: Spectrally resolved reflectance for selected nanocylinder coatings and a single layer ARC on InP and GaAs solar cells in an EVA encapsulant. (a) and (b) show the reflectance spectra for the TiO_2 NCs (blue), ITO NCs (red), and Si_3N_4 ARC (green), as well as including the reflectance offset from the glass-air interface at the front of the module (black dashed line). (c) and (d) show results for the TiO_2 NCs and Si_3N_4 ARC in EVA (solid lines) and air (dot-dashed lines).

examining Figure 4.4 parts (c) and (d), which compare the TiO_2 NC and Si_3N_4 coatings in air and EVA. In air, the coatings are able to fully minimize the reflectance, but tend to have large reflectance tails which decrease the antireflection effects of the coatings at large wavelengths. While the coatings in EVA do not perform as well as in air, they seem to have flatter reflectance spectra, and thus more broadband

71
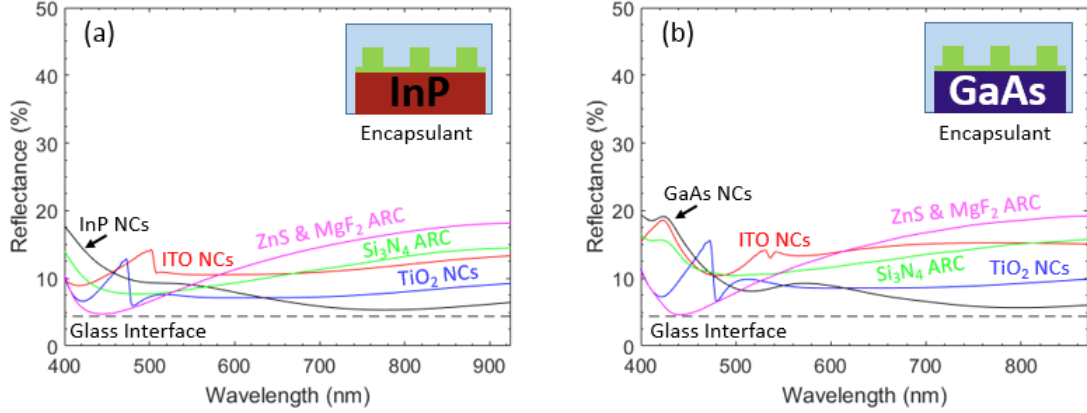
Figure 4.5: Spectrally resolved reflectance for various coating structures on InP and GaAs solar cells in an EVA encapsulant. (a) and (b) show the reflectance spectra for the active materials NCs (black solid line), TiO_2 NCs (blue), ITO NCs (red), Si_3N_4 ARC (green), and ZnS & MgF_2 dual layer ARC (magenta), as well as including the reflectance offset from the glass-air interface at the front of the module (black dashed line).

Table 4.2: Solar-weighted reflectivity ($R_{AM1.5G}$) for all optimized ARCs on InP and GaAs in EVA. Note - these values include the 4.4 % reflectance offset at the glass-air interface at the top of the module.

	$R_{AM1.5G}$ for optimized coatings in EVA				
Substrate Material	Substrate NCs	ITO NCs	TiO_2 NCs	Si_3N_4 ARC	ZnS & MgF_2 ARC
InP	11.41 %	11.27 %	9.54 %	11.40 %	11.90 %
GaAs	12.94 %	13.39 %	10.91 %	13.91 %	12.61 %

and wavelength-insensitive behavior. The feature in the reflectance spectra of the NC coatings for wavelengths < 500 nm is due in part to the onset of backscattered diffraction orders at these wavelengths.

When comparing these results against the active material NCs and the optimized dual layer ARC, we can see a few interesting trends (Figure 4.5). For example, the dual layer ARC in EVA has a reflectance spectrum similar to that of a single layer

72

Table 4.3: Solar-weighted absorptivity ($A_{AM1.5G}$) for optimized NCs on InP and GaAs in EVA. Note - these values include the 4.4 % reflectance offset at the glass-air interface at the top of the module.

		$A_{AM1.5G}$ for optimized NCs		
Substrate Material	NC Material	Total	In substrate	In coating
InP	ITO	88.73 %	76.53 %	12.20 %
	TiO$_2$	90.46 %	83.83 %	6.63 %
GaAs	ITO	86.61 %	71.28 %	15.33 %
	TiO$_2$	89.09 %	81.51 %	7.58 %

ARC in air (see Figure 2.10). This is not surprising though, because the top layer of the dual layer ARC, MgF$_2$ has an index of ~ 1.4 over the relevant spectrum, while EVA has an index of ~ 1.5 over the same spectral range. EVA's index is almost identical to the glass layer at the top surface of the module, and is so close to that of the MgF$_2$ that the dual layer ARC in EVA acts like an effective single layer coating. Additionally, the active material NCs seem to have significant reflectance suppression at long wavelengths in EVA which is not necessarily present in air. One possible cause of this effect could simply be the difference in index contrast from the air/active material interface versus the EVA/active material interface. Finally, we can see qualitatively that the TiO$_2$ NC coating still has the best overall reflectance supression across the entire spectral range.

As in previous chapters, we can take the spectrally resolved reflectance of our structures in EVA and convert them to a solar-weighted reflectance via Equation 2.1. We can see from the results in Table 4.2 that even though the results are much higher than these structures in air, the nanocylinder coatings still outperform
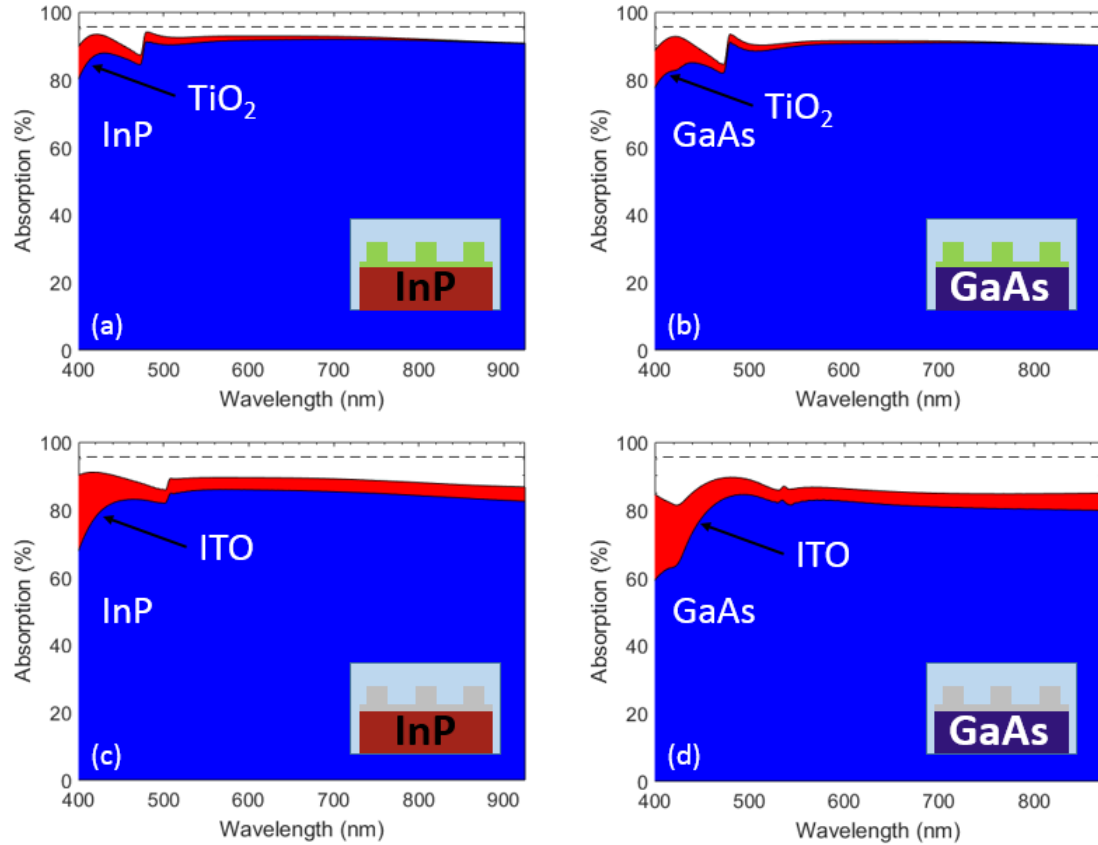
Figure 4.6: Spectrally resolved absorption in the NC coating and substrate layers for the TiO$_2$ NC and ITO NC coatings on InP and GaAs in EVA. (a) and (b) show the results for the TiO$_2$ NC coatings on InP and GaAs, respectively. (c) and (d) show the results for the ITO NC coatings on InP and GaAs respectively. The blue region represents the absorption in the substrate while the red region represents the absorption in the NC coating layer. The black dashed line represents the 4.4 % absorption decrease due to reflection at the glass-air front interface.

both the single and dual layer ARCs, even in EVA. It is also important to note that these reflectances are a bit inflated due to the 4.4 % reflectance offset at the top surface of the module structure. So the solar-weighted reflectivity for the optimized TiO$_2$ NCs increased from 1.3 % at the air/TiO$_2$ interface (Table 2.2) to 5.1 % at the EVA/TiO$_2$ interface (Table 4.2). Overall, this is not an extremely significant

74

increase in $R_{AM1.5G}$ and the broadband reflectance suppresion of the NC coatings in EVA may end up being an added benefit of using these coatings in realistic module configurations of solar cells.

We do not want to be misled by these low solar-weighted reflectance values from these structures, however, so we again perform simulations such as those described in Chapter 2 to determine the solar-weighted absorption in each layer for these devices in EVA (Figure 4.6). We can also see the quantitative results, summarized in Table 4.3. As with previous results, there is significant absorption in the ITO NC coatings, which decreases the amount of absorption we can theoretically achieve in the substrate. Also consistent with previous results, there is more absorption in the coating layers at short wavelengths and consistent absorption across the entire spectrum for the ITO NC coatings, regardless of substrate material.

4.3 Discussion

In this chapter we have seen that solar cells with our nanostructured coatings have the potential to perform extremely well, with potential efficiencies rivaling that of world record solar cells. We have also seen that these structures still perform well optically even when being placed in a module-like architecture, surrounded by an encapsulant instead of air. Further studies to optimize these nanostructures within an encapsulant could reveal the versatility of these types of nanophotonic coatings on different materials and in different optical environments. Overall, the thin-film devices with the nanostructured TiO$_2$ coatings show vastly improved performance

compared to both the bare substrate material and the single and dual layer ARCs.

Chapter 5:   Conclusions and Future Work

In this chapter we summarize the main conclusions that can be drawn from this work, as well as present options for future work which can build on our results.

5.1   Conclusions

In this thesis we have presented designs of novel nanostructured anitreflection coatings for high performance III-V thin-film solar cells consisting of periodic arrays of nanocylinders. The nanocylinders can be made of many different materials, though the arrays we designed focused on nanostructures of the active photovoltaic material, TiO_2, and ITO for reasons such as low surface recombination, previous work with Si, and fabrication considerations, respectively. These nanophotonic structures are used primarily as antireflection coatings which enhance the solar cell's overall optoelectronic performance. Geometric optimizations utilizing solar-weighted reflectance as a figure of merit as well as spectrally resolved reflectance studies have shown that these structures, when properly optimized, can have a solar-weighted average reflectance of 1.3 %, outperforming traditional antireflection coatings. We were also able to explore the absorption in the substrate and coating layers to validate the reflectance results, and found that the ITO NC coatings suf-

fered from large parasitic absorption in the ITO layer, preventing more light from being absorbed in the substrate. Overall the TiO_2 NC coatings had the best optical performance with minimal parasitic absorption, showing that these NC coatings have potential use beyond the Si materials systems with which they have been previously utilized.

By investigating the field intensity profiles and optical modes of these nanostructured coatings, we found that the optical enhancement provided by the coatings is primarily due to the coupling between Mie-like resonances and thin-film interference effects. The nanoclyinder arrays act as a thin-film dielectric layer of an efffective refractive index, providing additional enhancement compared to a typical single or dual layer ARC. Additionally, the highest performing nanostructures do not require modification of the absorber layer, which may help reduce complexity and cost, while simultaneously limiting the negative effects of increased surface recombination. We used results from optical simulations with a device-like architecture as inputs into electrical simulations, which allowed us to explore the possible solar cell device parameters of fully functional devices utilizing our coatings. We discovered that these nanostructured optical coatings can push the efficiency of InP cells to $>$ 23 %, with similar results expected for GaAs but with possibly higher efficiencies. By using inexpensive industrial fabrication processes such as nanoimprint lithography, these types of structures can be fabricated on other high-index substrates, thus continuing to push the limits of photovoltaic performance.

5.2 Future Work: Fabrication, Testing, and Measurement

The primary goal of future work with this project is to fabricate these structures on already-functional solar cells and take measurements to quantify the optoelectronic characteristics of real devices. As stated previously, we had considered fabricating the nanostructures on these cells via FIB, and this is likely the route we would take in fabricating the structures we have designed here. From our studies of ITO NCs, we have seen that though there is large absorption in the ITO, there is not a significant decrease in overall optical performance. We would likely deposit TiO$_2$ on bare InP and GaAs via electron beam deposition, and then deposit small, thin layers of ITO to facilitate the transport of excess charge during FIB processing. Once the nanocylinder arrays were fabricated we would use a solar simulator and voltage and current probes to measure the electrical response of the cells to an AM1.5G solar spectrum, obtaining J-V characteristics. We would then take optical measurements in our lab with setups we currently have, such as spectrally resolved reflectance, angularly resolved reflectance, and external quantum efficiency (EQE). We would also perform all of these measurements and tests on the original cells in order to have a control set of data for comparison. These measurements and experiments would provide us with a set of experimental results we could compare to the computational and theoretical results of this work, ideally further validating the advantages of these nanocylinder coatings on III-V thin-film solar cells.

Appendix A: Additional Results and Figures

Here we include a few additional figures and results.

Figure A.1: Geometry sweeps of $h = 50$ nm active material nanocylinders in (a) InP and (b) GaAs. Both (a) and (b) show the optimized geometry, indicated by the black diamond.

Figure A.2: Geometry sweeps of $h = 150$ nm active material nanocylinders in (a) InP and (b) GaAs. Both (a) and (b) show the optimized geometry, indicated by the black diamond.
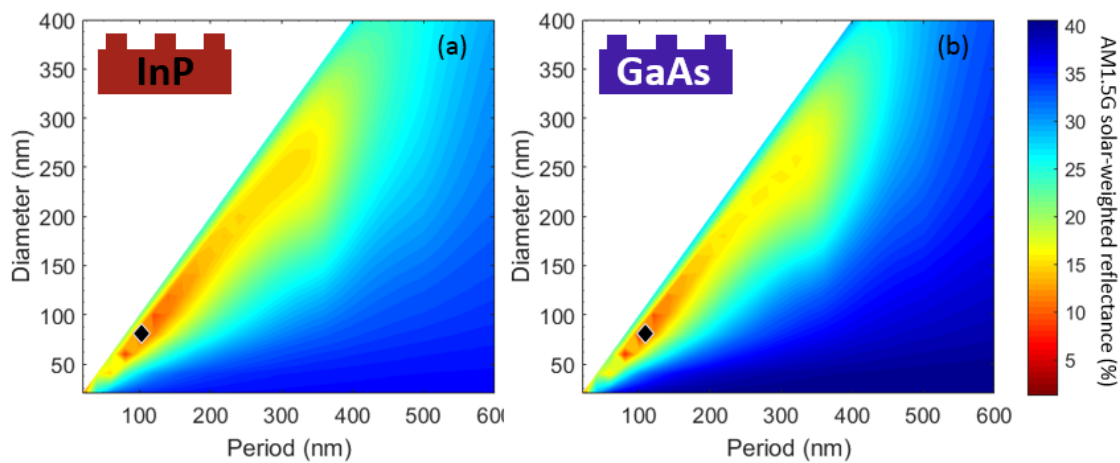

Figure A.3: Geometry sweeps of $h = 200$ nm active material nanocylinders in (a) InP and (b) GaAs. Both (a) and (b) show the optimized geometry, indicated by the black diamond.
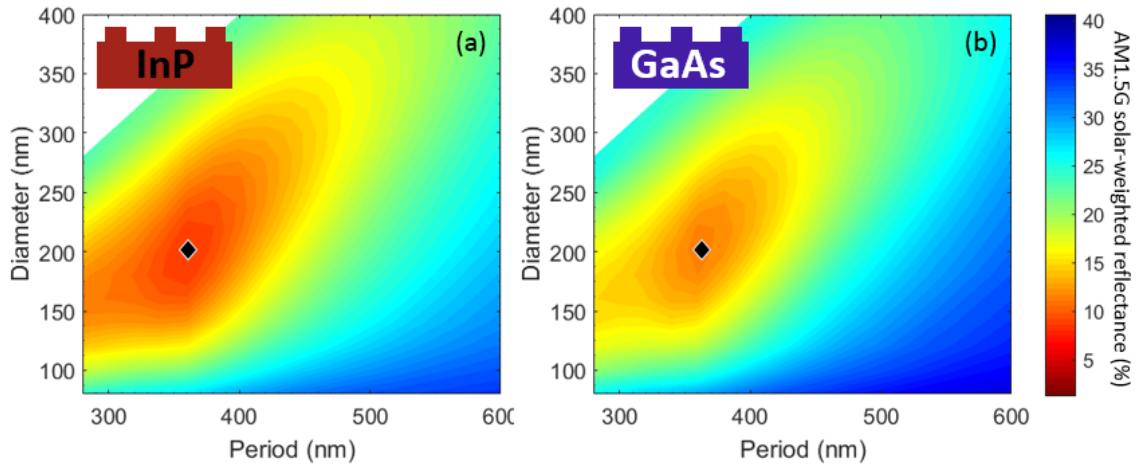
Table A.1: Optimized geometries of active material nanocylinder coatings on InP and GaAs. Solar-weighted reflectivities of these structures can be found in Table 2.1.

Substrate Material	NC Height (nm)	NC Period (nm)	NC Diameter (nm)
InP	50	100	80
	100	180	120
	150	360	200
	200	380	200
GaAs	50	100	80
	100	180	120
	150	360	200
	200	400	220
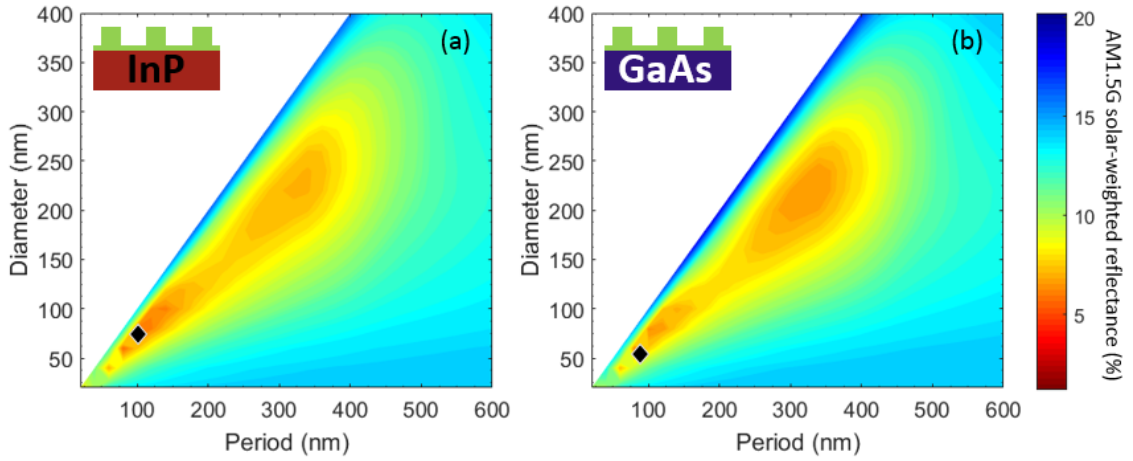
Figure A.4: Geometry sweeps of $h = 50$ nm TiO$_2$ nanocylinders on (a) InP and (b) GaAs. Both (a) and (b) show the optimized geometry, indicated by the black diamond.
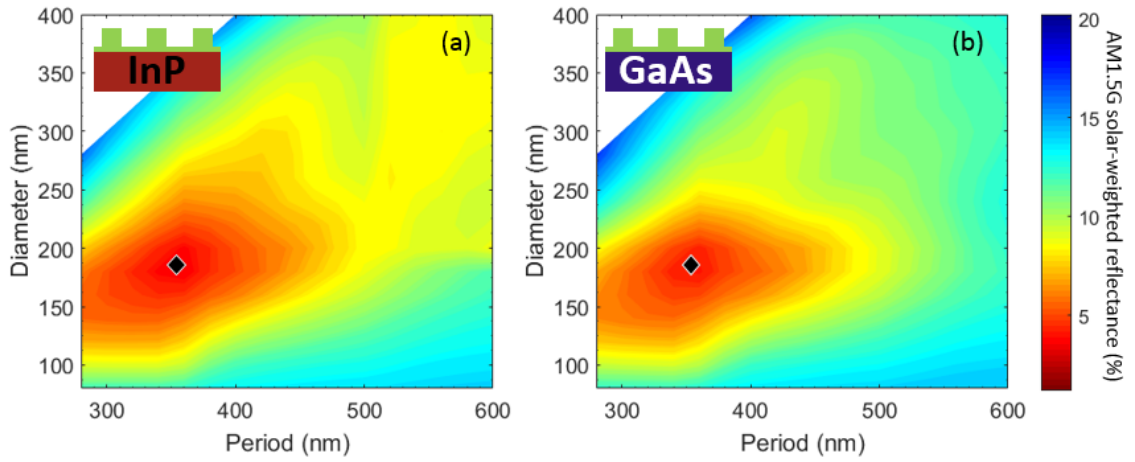
Figure A.5: Geometry sweeps of $h = 150$ nm TiO_2 nanocylinders on (a) InP and (b) GaAs. Both (a) and (b) show the optimized geometry, indicated by the black diamond.
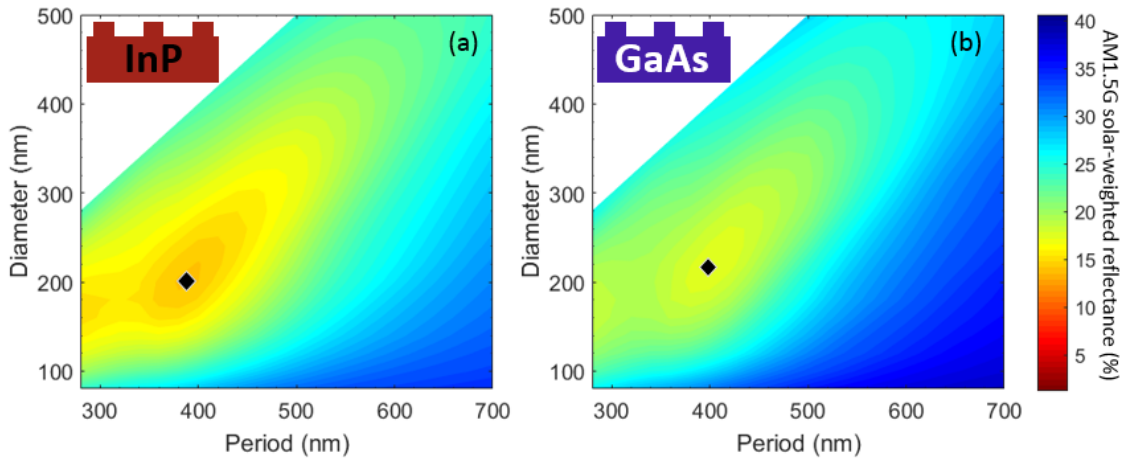

Figure A.6: Geometry sweeps of $h = 200$ nm TiO_2 nanocylinders on (a) InP and (b) GaAs. Both (a) and (b) show the optimized geometry, indicated by the black diamond.

Table A.2: Optimized geometries of TiO$_2$ nanocylinder coatings on InP and GaAs. Solar-weighted reflectivities of these structures can be found in Table 2.2.

| Substrate Material	NC Height (nm)	NC Period (nm)	NC Diameter (nm)
InP	50	100	80
	100	320	180
	150	360	180
	200	400	220
GaAs	50	80	60
	100	320	180
	150	360	180
	200	380	200

Figure A.7: Geometry sweeps of $h = 50$ nm ITO nanocylinders on (a) InP and (b) GaAs. Both (a) and (b) show the optimized geometry, indicated by the black diamond.

Figure A.8: Geometry sweeps of $h = 150$ nm ITO nanocylinders on (a) InP and $h = 100$ nm ITO NCs on (b) GaAs. Both (a) and (b) show the optimized geometry, indicated by the black diamond.
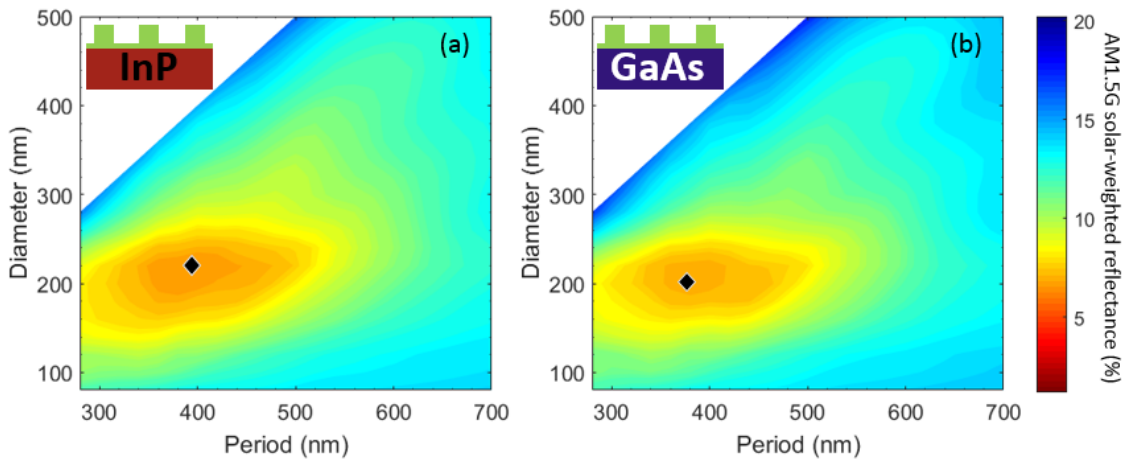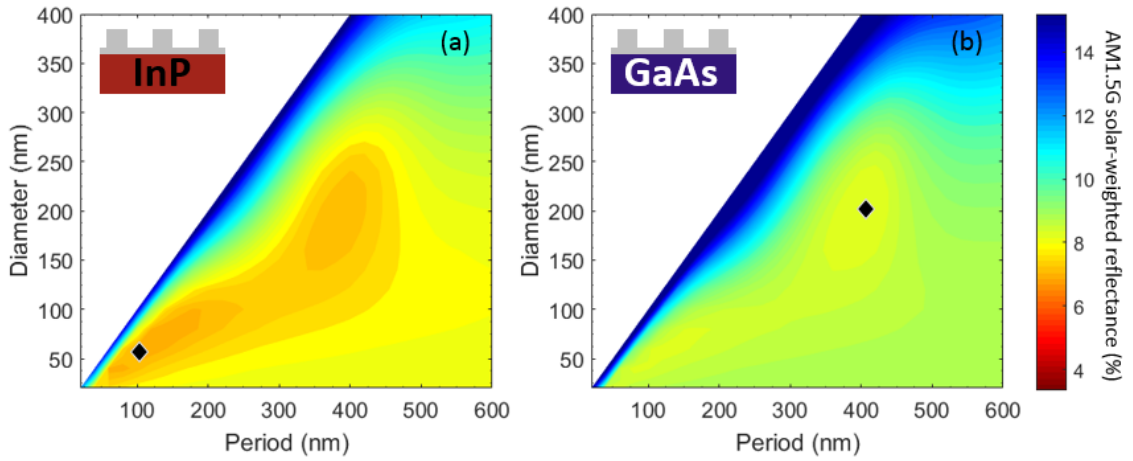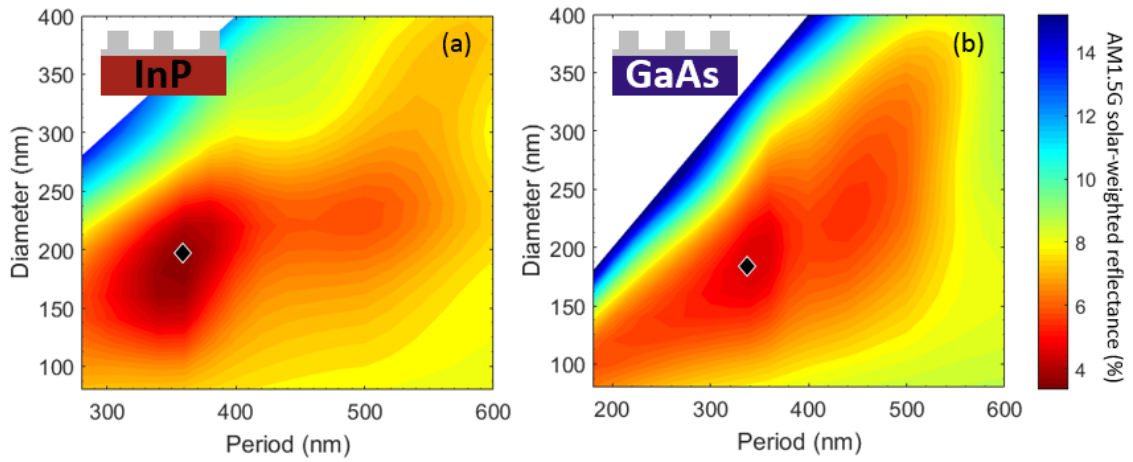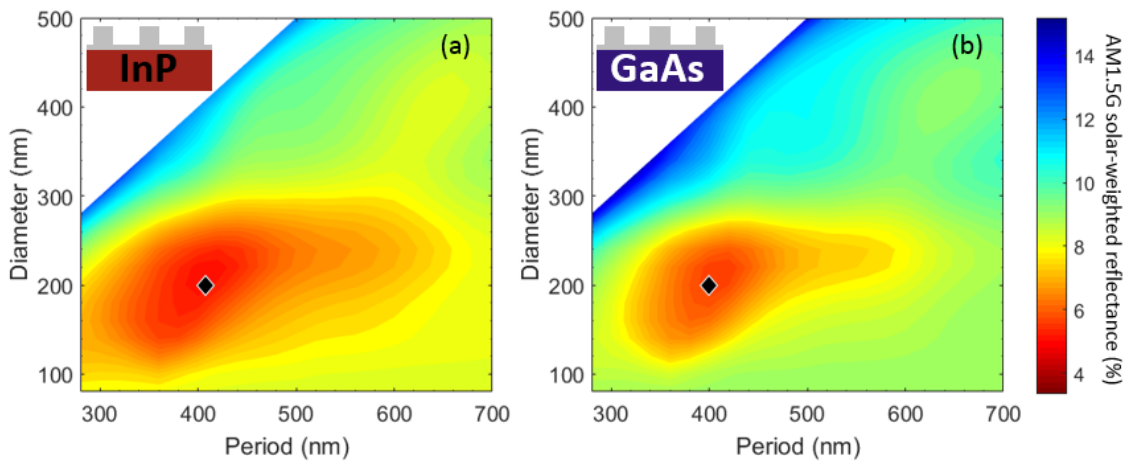

Figure A.9: Geometry sweeps of $h = 200$ nm ITO nanocylinders on (a) InP and (b) GaAs. Both (a) and (b) show the optimized geometry, indicated by the black diamond.

Table A.3: Optimized geometries of ITO nanocylinder coatings on InP and GaAs. Solar-weighted reflectivities of these structures can be found in Table 2.4.

Substrate Material	NC Height (nm)	NC Period (nm)	NC Diameter (nm)
InP	50	100	60
	100	340	180
	150	360	200
	200	400	200
GaAs	50	400	200
	100	340	180
	150	360	200
	200	400	200
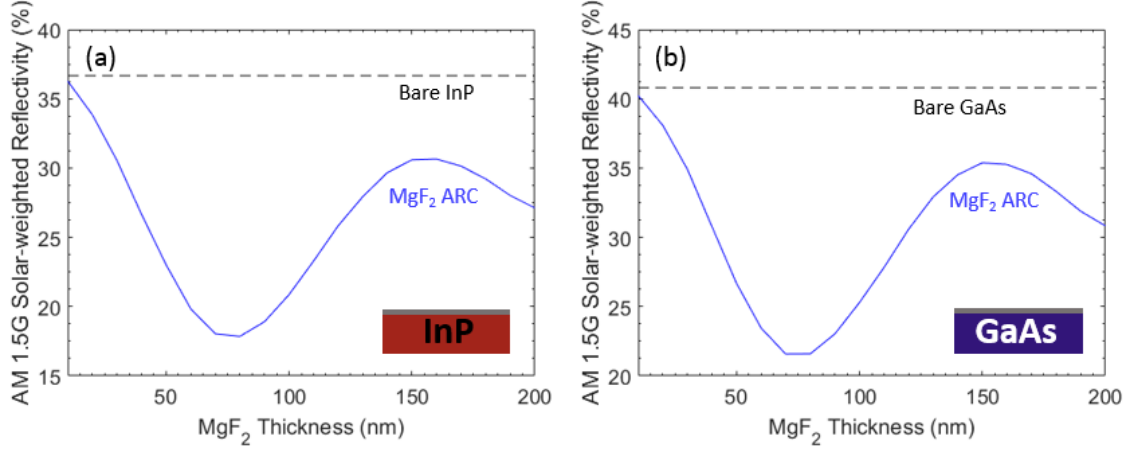
Figure A.10: Solar-weighted reflectivity of a single layer MgF$_2$ ARC on (a) InP and (b) GaAs for varying thicknesses of the coating layer. For (a) and (b) the black dashed line indicates the $R_{AM1.5G}$ of the bare substrate material and the blue line represents the device with the coating, in this case MgF$_2$.

Bibliography

[1] K. Jger, M. Fischer, R. A. C. M. M. van Swaaij, and M. Zeman "A scattering model for nano-textured interfaces and its application in opto-electrical simulations of thin-film silicon solar cells," J. Appl. Phys. **111**(8), 083108 (2012).

[2] M. Boccard, C. Battaglia, S. Hnni, K. Sderstrm, J. Escarr, S. Nicolay, F. Meillaud, M. Despeisse, and C. Ballif, "Multiscale Transparent Electrode Architecture for Efficient Light Management and Carrier Collection in Solar Cells," Nano Lett. **12**(3), 13441348 (2012).

[3] M. L. Brongersma, Y. Cui, and S. Fan, "Light management for photovoltaics using high-index nanostructures," Nat. Mater. **13**(5), 451460 (2014).

[4] C. E. R. Disney, S. Pillai, C. M. Johnson, and M. A. Green, "Self-Assembled Nanostructured Rear Reflector Designs for Thin-Film Solar Cells," ACS Photonics **2**(8), 11081116 (2015).

[5] L. Zeng, P. Bermel, Y. Yi, B. A. Alamariu, K. A. Broderick, J. Liu, C. Hong, X. Duan, J. Joannopoulos, and L. C. Kimerling, "Demonstration of enhanced absorption in thin film Si solar cells with textured photonic crystal back reflector," Appl. Phys. Lett. **93**(22), 221105 (2008).

[6] P. Bermel, C. Luo, L. Zeng, L. C. Kimerling, and J. D. Joannopoulos, "Improving thin-film crystalline silicon solar cell efficiencies with photonic crystals," Opt. Express **15**(25), 1698617000 (2007).

[7] J. N. Munday and H. A. Atwater, "Large integrated absorption enhancement in plasmonic solar cells by combining metallic gratings and antireflection coatings," Nano Lett. **11**(6), 21952201 (2011).

[8] H. R. Stuart and D. G. Hall, "Absorption enhancement in silicon-on-insulator waveguides using metal island films," Appl. Phys. Lett. **69**(16), 23272329 (1996).

[9] V. E. Ferry, J. N. Munday, and H. A. Atwater, "Design considerations for plasmonic photovoltaics," Adv. Mater. **22**(43), 47944808 (2010).

[10] K. R. Catchpole and A. Polman, "Plasmonic solar cells," Opt. Express **16**(26), 2179321800 (2008).

[11] R. Santbergen, H. Tan, M. Zeman, and A. H. M. Smets, "Enhancing the driving field for plasmonic nanoparticles in thin-film solar cells," Opt. Express **22**(S4), A1023A1028 (2014).

[12] P. Spinelli, M. A. Verschuuren, and A. Polman, "Broadband omnidirectional antireflection coating based on subwavelength surface Mie resonators," Nat. Commun. **3**, 692 (2012).

[13] F. J. Bezares, J. P. Long, O. J. Glembocki, J. Guo, R. W. Rendell, R. Kasica, L. Shirey, J. C. Owrutsky, and J. D. Caldwell, "Mie resonance-enhanced light absorption in periodic silicon nanopillar arrays," Opt. Express **21**(23), 2758727601 (2013).

[14] D. Shir, J. Yoon, D. Chanda, J. H. Ryu, and J. A. Rogers, "Performance of ultrathin silicon solar microcells with nanostructures of relief formed by soft imprint lithography for broad band absorption enhancement," Nano Lett. **10**(8), 30413046 (2010).

[15] P. Spinelli and A. Polman, "Light Trapping in Thin Crystalline Si Solar Cells Using Surface Mie Scatterers," IEEE J. Photovoltaics **4**(2), 554559 (2014).

[16] M. A. Green, "Radiative efficiency of state-of-the-art photovoltaic cells," Prog. Photovolt. Res. Appl. **20**(472), 611 (2012).

[17] I. Schnitzer, E. Yablonovitch, C. Caneau, and T. J. Gmitter, "Ultrahigh spontaneous emission quantum efficiency, 99.7% internally and 72% externally, from AlGaAs/GaAs/AlGaAs double heterostructures," Appl. Phys. Lett. **62**(2), 131133 (1993).

[18] O. D. Miller, E. Yablonovitch, and S. R. Kurtz, "Intense internal and external fluorescence as solar cell approach the SQ efficiency limit," IEEE J. Photovoltaics **2**(3), 127 (2012).

[19] D. E. Aspnes and A. A. Studna, "Dielectric functions and optical parameters of Si, Ge, GaP, GaAs, GaSb, InP, InAs, and InSb from 1.5 to 6.0 eV," Phys. Rev. B **27**(2), 9851009 (1983).

[20] M. A. Green, K. Emery, Y. Hishikawa, W. Warta, and E. D. Dunlop, "Solar cell efficiency tables (version 46)," Prog. Photovolt. Res. Appl. **23**(7), 805812 (2015).

[21] B. M. Kayes, H. Nie, R. Twist, S. G. Spruytte, F. Reinhardt, I. C. Kizilyalli, and G. S. Higashi, "27.6% Conversion efficiency, a new record for single-junction solar cells under 1 sun illumination," in *Conference Record of the Thirty Second IEEE Photovoltaic Specialists Conference* (IEEE, 2011), pp. 00000400008.

[22] C. J. Keavney, V. E. Haven, and S. M. Vernon, "Emitter Structures in MOCVD InP Solar Cells," in *Conference Record of the Twenty First IEEE Photovoltaic Specialists Conference* (IEEE, 1990), pp. 141144.

[23] Y. Xu, T. Gong, and J. N. Munday, "The generalized Shockley-Queisser limit for nanostructured solar cells," Sci. Rep. **5**, 13536 (2015).

[24] Y. Da and Y. Xuan, "Role of surface recombination in affecting the efficiency of nanostructured thin-film solar cells," Opt. Express **21**(S6), A1065A1077 (2013).

[25] N. Huang, S. Member, and M. L. Povinelli, "Design of Passivation Layers on Axial Junction GaAs Nanowire Solar Cells," IEEE J. Photovoltaics **4**(6), 15111517 (2014).

[26] B. Rastegar and J. F. Wager, "Surface recombination velocity and bulk lifetime in GaAs and InP," Semicond. Sci. Technol. **1**(3), 207212 (1986).

[27] J. Wallentin, N. Anttu, D. Asoli, M. Huffman, I. Aberg, M. H. Magnusson, G. Siefer, P. Fuss-Kailuweit, F. Dimroth, B. Witzigmann, H. Q. Xu, L. Samuelson, K. Deppert, and M. T. Borgstrm, "InP nanowire array solar cells achieving 13.8% efficiency by exceeding the ray optics limit," Science **339**(6123), 10571060 (2013).

[28] M. T. Borgstrm, J. Wallentin, M. Heurlin, S. Flt, P. Wickert, J. Leene, M. H. Magnusson, K. Deppert, and L. Samuelson, "Nanowires with promise for photovoltaics," IEEE J. Sel. Top. Quantum Electron. **17**(4), 1050 1061 (2011).

[29] N. M. Shmidt, "Indium Phosphide (InP)," in *Handbook Series on Semiconductor Parameters*, vol. 1, M. Levinshtein, S. Rumyantsev, and M. Shur, eds. (World Scientific, 1996).

[30] J. R. DeVore, "Refractive Indices of Rutile and Sphalerite," J. Opt. Soc. Am. **41**(6), 416419 (1951).

[31] Y. Lin, R. Kapadia, J. Yang, M. Zheng, K. Chen, M. Hettick, X. Yin, C. Battaglia, I. D. Sharp, J. W. Ager, and A. Javey, "Role of TiO2 Surface Passivation on Improving the Performance of p-InP Photocathodes," J. Phys. Chem. C **119**, 2308 (2015).

[32] X. Yin, C. Battaglia, Y. Lin, K. Chen, M. Hettick, M. Zheng, C. Y. Chen, D. Kiriya, and A. Javey, "19.2% Efficient InP Heterojunction Solar Cell with Electron-Selective TiO2 Contact," ACS Photonics **1**(12), 12451250 (2014).

[33] P. Spinelli, B. Macco, M. A. Verschuuren, W. M. M. Kessels, and A. Polman, "Al2O3/TiO2 nano-pattern antireflection coating with ultralow surface recombination," Appl. Phys. Lett. **102**(23), 1013 (2013).

[34] D. Maystre, *Plasmonics: From Basics to Advanced Topics* (Springer, 2012), Chap. 2.

[35] P. Spinelli, F. Lenzmann, A. Weeber, and A. Polman, "Effect of EVA Encapsulation on Antireflection Properties of Mie nanoscatterers for c-Si Solar Cells," IEEE J. Photovoltaics **5**(2), 559564 (2015).